

Application of Ion Implantation to Fabricate Optical Waveguides

Feng Qiu

August, 2011

Abstract

This thesis describes the fabrication and characterization of ion implanted waveguides in chalcogenide glasses and neodymium-doped yttrium aluminum garnet (Nd:YAG) crystals. It is demonstrated that an optical waveguide can be obtained by a simple proton implantation in gallium lanthanum sulphide (GLS) glass. Two modes exist in the waveguide at a wavelength of 632.8 nm and the refractive index profile of the waveguide is reconstructed. The near-field pattern of the transmitted light is obtained, and the propagation loss is about 3.2 dB/cm. Based on the data of proton implanted waveguides, a titanium doped gallium lanthanum oxysulfide (Ti:GLSO) glass waveguide is fabricated by the double proton implantation. That waveguide does not exhibit tunneling effect, which is consistent with our design. Based on Raman analyses, we conclude that the glass matrix expansion due to nuclear damage causes the optical barrier formation. Little change in the guiding layer and low propagation loss present that Ti:GLSO glass waveguide may be a candidate of tunable lasers and has a possibility to take place of versatile but expensive Ti-sapphire lasers.

Swift-heavy ion implantation (SHI), as a novel technique to fabricate waveguides, is explored to form waveguides in GLS and GLSO glasses. A “well” region with increased refractive index (0.1% for GLS and 0.3% for GLSO) is formed near the surface of the glass based on the electronic energy deposition; a “barrier” layer with decreased refractive index is formed inside the glass due to the nuclear energy deposition. As a result, the waveguides exhibit a refractive index distribution of “well + barrier” type. It is supposed that the change in local structure order of the substrate causes the “well” formation. The propagation loss is 2.0 dB/cm

for GLS and 2.2 dB/cm for GLSO glass waveguide.

Then, a buried planar Nd:YAG waveguide is fabricated by 20MeV N ion implantation. From the Raman and optical characterization, it has been found that the refractive index has a larger increase when the crystal damage is heavier. According to our analysis, this crystal damage is caused by the electronic energy loss in the first several micrometers of irradiated regions, while nuclear energy loss also acts on the damage near the end of ion range. This work is helpful to understand the mechanisms of swift-heavy ion implanted Nd:YAG waveguide formation.

At last, planar waveguides are fabricated in Nd or Ho doped GLS laser glasses by 60MeV Ar or 20MeV N ion implantation. The Ar implanted waveguides exhibit an approximate step-like distribution, while the N implanted ones show a “well + barrier” type. This difference can be attributed to the much lower dose of Ar ions. After annealing, the N implanted waveguides can support two modes at 1539nm and have low propagation loss, which makes them as candidates for novel waveguide lasers.

TABLE OF CONTENTS

Chapter 1 Introduction.....	1
1.1 History review.....	1
1.2 Thesis motivation.....	3
Chapter 2 Fundamental concepts of ion implanted waveguides	5
2.1 Ion implantation technique	5
2.1.1 Ion implantation process	5
2.1.2 Electronic and nuclear damage	6
2.1.3 Optical effects of ion implantation.....	8
2.1.4 Conventional ion implantation and swift-heavy ion implantation	11
2.2 Light propagation in waveguides.....	12
2.2.1 Ray optics.....	12
2.2.2 Waveguide configuration	13
2.2.3 Electromagnetic analysis of a planar waveguide	14
2.3 Thermal-spike model	17
2.4 Chalcogenide glass and Nd:YAG crystal.....	21
2.4.1 Gallium lanthanum sulphide (GLS) glass	21
2.4.2 Metal elements doped GLS glass.....	22
2.4.3 Nd:YAG crystal.....	25
References.....	27
Chapter 3 Experimental methods	30
3.1 Prism coupling	30
3.2 Reflectivity calculation method	31
3.3 End-fire coupling system	35
3.4 Back-reflection method.....	37
3.5 Fourier transform infrared spectroscopy.....	38
3.6 Raman spectroscopy technique.....	39
3.6.1 Origins of Raman scattering	39
3.6.2 Renishaw Ramascope instrumentation	40
References.....	42
Chapter 4 Conventional ion implantation	43
4.1 Proton-implanted planar waveguide in GLS glass.....	43
4.1.1 Introduction.....	43
4.1.2 Experimental	44
4.1.3 Experimental Results and Discussion	44
4.1.4 Conclusions	49
4.2 Ion implanted Ti:GLSO glass waveguide as a candidate of tunable lasers.....	50
4.2.1 Introduction.....	50
4.2.2 Waveguide fabrication	51
4.2.3 Guiding property results.....	53
4.2.4 Raman spectra analysis	55
4.2.5 Conclusion	57

References.....	58
Chapter 5 Swift-heavy ion implantation.....	60
5.1 Application of swift-heavy ion implantation to the formation of chalcogenide glass waveguides.....	60
5.1.1 Introduction.....	60
5.1.2 Experimental	61
5.1.3 Results and Discussion.....	62
5.1.4 Conclusions.....	69
5.2 Refractive index change mechanisms in swift -heavy ion implanted Nd:YAG waveguide	69
5.2.1 Introduction.....	69
5.2.2 Experimental	70
5.2.3 Optical and Raman characterization	71
5.2.4 Theoretical damage comparison	75
5.2.5 Conclusions.....	78
5.3 Swift and Heavy Ion Implanted rare-earth doped GLS Laser Glass Waveguides and Their Different Refractive Index Distributions	78
5.3.1 Introduction.....	78
5.3.2 Experimental	79
5.3.3 60MeV Ar implanted waveguides.....	79
5.3.4 20MeV N implanted waveguides.....	81
5.3.5 Discussion of refractive index distributions.....	85
5.3.6 Conclusions.....	87
References.....	88
Chapter 6 Conclusions.....	92

Chapter 1 Introduction

1.1 History review

Optical communication has been changing this world tremendously. Everyday, many people are now logging-on to the Internet and the World Wide Web, which has become a part of daily life. In many localities, fibers to the home and integrated service digital networks have become realities.

One of the world's earliest optical telecommunication systems was build up in ancient China about three thousand years ago, known as "Smoking & Fire Towers". Since Alexander Graham Bell's invention of the telephone in 1876, communications experienced revolutionary developments. Also, it was Bell himself who invented one of the earliest light-wave communication devices in 1880, just four years after the invention of the telephone. But incoherent light and its free-space transmission through the atmosphere made the photo-phone impractical for long-distance communications. The advents of lasers in 1960 and low-loss optical fiber in 1970's eliminated all these barriers.

Although the losses of signals in optical fibers approach 0.1dB/km and dispersion can be controlled effectively, the optical signal has to be converted back to electronic to be understood by every appliances, such as telephones, faxes, and computers. This is where integrated optics makes it appearance. The concept of integrated optics was coined by S.E. Miller to emphasize the similarities between planar optical circuit technology and the well known integrated electronics technology, while wires and radio links are replaced by optical waveguides. It is a technology with the ability of integrating various optical devices and

components (such as amplifiers, lasers, modulators and et. al) on a single substrate (chip). So far, integrated optics is in development and realization of high quality waveguides in different optical materials is still on the way.

An optical waveguide is characterized by a region with high refractive index surrounded by regions with lower index. Except for integrating many components on one chip, some properties of substrate materials can be considerably improved relative to those of the corresponding bulks. For example, laser generation in waveguides has a lower pumping threshold, and photorefractive waveguides usually have a faster response than the bulk components. Moreover, the components based on waveguides may be connected together with optical fibers quite simply because the dimensions of waveguides are directly compatible with fibers used in telecommunications.

There are several methods which may be employed for fabrication of optical waveguides, such as thin film deposition, ion exchange, ion implantation and so on. Among these techniques, ion implantation possesses one of the most advantageous characteristics, that is, the wide applicability of materials. The first ion implanted waveguide fabricated was reported in 1968 in fused silica. Since then, ion implantation has been confirmed to be a universal method of fabricating waveguides in many kinds of substrates (more than 100 optical materials). On the other hand, we can easily control the refractive index profiles of the substrates by adjusting the implantation parameters and the waveguide geometries by adding masks, and further optimize waveguide properties by post implantation treatments (e.g. conventional or rapid thermal annealing,).

1.2 Thesis motivation

So far, silica glass is the most favorable material for long distance optical fiber telecommunications. However, there are aspects of the properties of silica which make it unsuitable for certain applications. For instance the low rare earth solubility of silica means that the interaction length of active devices based on rare-earth doped silica is relatively long. The high phonon energy of silica means that transitions of many rare earth dopants decay non-radiatively. The relatively low non-linear refractive index of silica means that non-linear devices based on silica require relatively high intensities in order to function. The transmission wavelength of silica is also limited to 2 μm .

Gallium lanthanum sulphide (GLS) glass can overcome the above shortcomings of silica. The comparisons of main properties of two kinds of glasses are listed in table I. The detailed description of GLS and rare-earth doped GLS glass properties is exhibited in section 2.4.

Table I Optical properties of Silica and GLS

Optical property	Silica	GLS
Refractive index (633nm)	1.425	2.446
Nonlinear index ($10^{-20}\text{m}^2\text{W}^{-1}$)	2.5	300
Transmission window (μm)	0.16-2.0	0.5-10
Phonon energy (cm^{-1})	1150	425

Although ion implanted waveguides have been studied for more than 40 years, there is few research on chalcogenide glasses. In this work, conventional ion implantation and swift-heavy ion implantation are applied to fabricate waveguides in GLS and metal elements doped GLS glasses, which shows promise for the development of optical devices

based on these waveguide structures.

Regarding the mechanisms of ion implanted waveguide formation, there is not a universal explanation for all materials. However, the mechanisms are quite important to design and fabricate waveguides. For example, for laser crystal and glass, we expect the waveguide keeping the original properties as the substrate; otherwise the emission wavelength and intensity may be damaged. Thus, the waveguide formation mechanism is quite useful for us to choose suitable implantation parameters. In section 4.2 and 5.2, the mechanisms of proton implanted Ti doped GLS glass waveguide and swift-heavy ion implanted Nd:YAG waveguide are studied respectively. Both of them are helpful to understand the effects of ion implantation on the damage of the substrates and to fabricate high quality waveguide lasers.

Chapter 2 Fundamental concepts of ion implanted waveguides

2.1 Ion implantation technique

The fabrication of optical waveguides in crystals and glasses using ion implantation technique has been a topic of great interest for over the last four decades [1, 2]. The increasing availability of particle accelerators from their use in the semiconductor industry has resulted in ion implantation becoming popular as a method of fabricating planar waveguides. Here, we will overview ion implantation process and the mechanics of ion stopping in materials, and then go over the optical effects of ion implantation.

2.1.1 Ion implantation process

Ion implantation is a material engineering process by which ions of a material with desired energy are impacted into another solid. Energetic ions are produced in an ion source, accelerated by an accelerator and directed as a beam into the target (Fig. 2.1.1). Virtually any element can be injected into the near-surface region of any solid substrate. Commonly implanted substrates include crystals, glasses, ceramics and polymers.

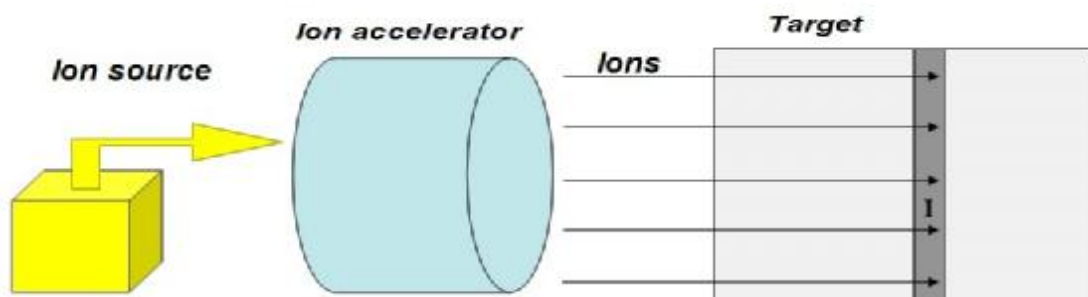


Fig. 2.1.1 Schematic of the ion implantation process

In the common ion implantation process, a beam of positively charged ions of the desired element is formed. Beam formation of a gas occurs by feeding a gas into an ion source. In the ion source, electrons, emitted from a hot filament, ionize the gas to form plasma, which is performed for the purpose of acceleration. Application of an electrostatic field results in the acceleration of the positive ions at high energies under high vacuum. The ions penetrate the target surface and stop at some position (region I in Fig. 2.1.1).

Forming a beam of a solid element (e.g. metals) usually uses the following two methods. The first method is commonly used in the semiconductor industry, which requires extremely high-purity beams. In this method, a reactive gas, such as chlorine, is used to form the plasma. A metal chloride is generated as the chlorine ions chemically react with the metal walls of the ion source. The metal chloride then is ionized to form plasma of metal and chlorine ions. An analyzing magnet is used to separate the chlorine ions from the desired metal ion beam. The second method employs sputtering to generate metal ions. In this method, inert argon gas is ionized. The positively charged ions are attracted to a negatively biased metal target. As the argon ions strike the target, pure metal atoms and ions are dislodged from the target. The metal ions are extracted and focused into a beam.

An ion implantation process is mainly determined by five process parameters: ion species, beam energy, implantation dose, tilt and twist angle (between ion beam and target).

2.1.2 Electronic and nuclear damage

When an energetic ion is implanted into a target, it will lose its energy by electronic and nuclear damage [3]. The nature of electronic energy loss is complicated and varies with different species of projectile and target. In summary, there are four main sources of electronic energy loss as the ion

travels through the material, each of which has a varying impact on slowing the ion and affecting the ion trajectory. These electronic stopping mechanisms can be divided as [4]:

- (1) excitation of band-electrons and conduction-electrons, i.e. weakly bound target electrons
- (2) direct kinetic energy transfer to the target electrons, i.e. electron-electron interactions
- (3) ionization of target atoms, i.e. promotion of localized (strongly bound) target electrons
- (4) excitation and ionization of the projectile itself.

As the ion slows down to the speed of sound (phonon speed), it is traveling slowly enough for the target atom nucleus to react to the Coulomb forces. The transfer of kinetic energy from the ion to the target atom is governed by straightforward two-body collision, which is nuclear energy loss.

The evolution of expressions for the nuclear and electronic energy loss has changed throughout the years, from the models put forth by Bohr [5], to more sophisticated semi-empirical model such as the Lindhard, Scharff, Schiott (LSS) theory [6], with refinements brought on by the advent of computers and numerical method techniques in modeling software such as Stopping Ranges of Ions in Matter (SRIM) [7]. By using the Monte Carlo simulation package SRIM, in which implanted ions are followed individually through their collisions in the target, all the important information can be calculated, such as implanted ion range, energy loss and so on. An example, figure 2.1.2 shows the energy loss (dE/dx) of 500keV proton implanted in LiNbO_3 . In this figure, we can obtain the nuclear and electronic energy loss per implanted proton. Note the scale of vertical coordinate between two kinds of energy loss is different. Note that the nuclear damage (energy loss) is usually dominant at the end of ion range, while the electronic damage (energy loss) plays a key role near the surface.

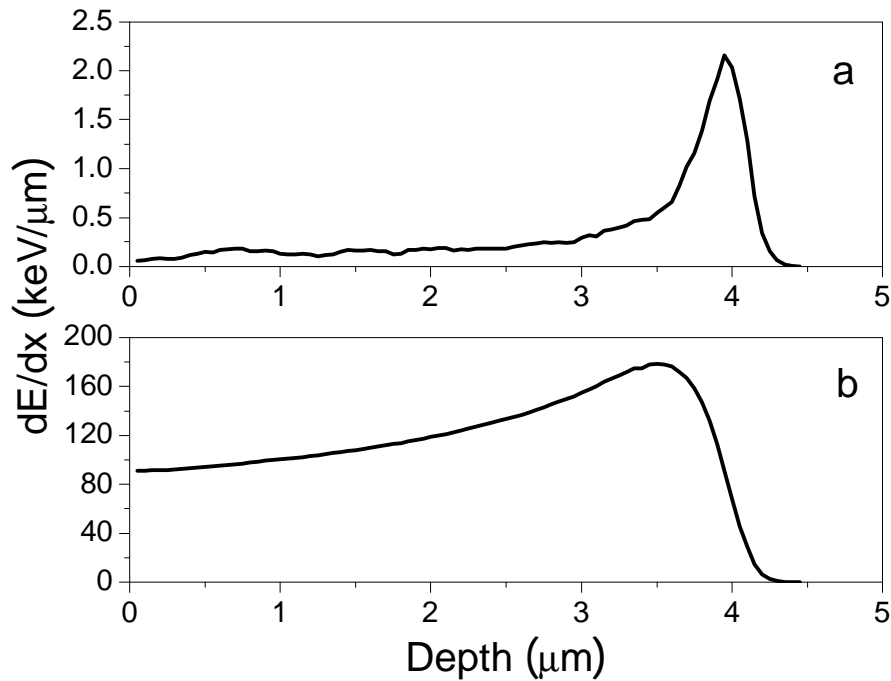


Fig. 2.1.2 (a) Nuclear and (b) electronic energy loss of 500keV proton in LiNbO₃

2.1.3 Optical effects of ion implantation

The requirement of generating a waveguide in a substrate is that a region of relatively high refractive index should be surrounded by regions of lower index. Permanent refractive index changes induced by ion implantation have been found in a wide range of materials. The general effects of ion implantation contributing towards the substrate refractive index change can be summarized as follows [8]:

- (1) Index change may be caused by lattice relaxation or the production of new phases.
- (2) Index change may be produced by the effects of stress.
- (3) Index change may occur due to the radiation-induced migration of substrate atoms.

These are general effects and there are other effects which can also cause refractive index change, such as photodarkening and photobleaching [9]. All

these effects depend on the type of substrates and implantation parameters.

Ion implantation in insulating materials always changes the refractive index and, depending on the target material, can either increase or reduce the value of the index. Thus, the refractive index profiles of ion implanted waveguides usually can be divided into two types: “barrier confinement” and “well + barriers” [10]. As shown in Fig. 2.1.3, the barrier refers to low refractive index layers buried inside the substrate generated by nuclear damage. The implantation can cause relatively large positive refractive index change in the near-surface region, resulting in an enhanced index well (Fig. 2.1.3 (a)). In this case, the light can be confined in this well even the barrier is quite narrow and with small refractive index decrease. This type usually happens for heavy (medium-mass) ion implantation with energy of several MeV.

For the barrier confinement (Fig. 2.1.3(b)), the electronic damage induces no change or only slight refractive index change between the surface and the barrier. In this way, this region with little index change is surrounded by low-index regions, which acts as a waveguide. However, the barrier should be thick enough otherwise the light will leak to the substrate. These barrier-confinement refractive index distributions are quite typical for ion-implanted waveguides in various materials, and are particularly common for those related to light ion implantation.

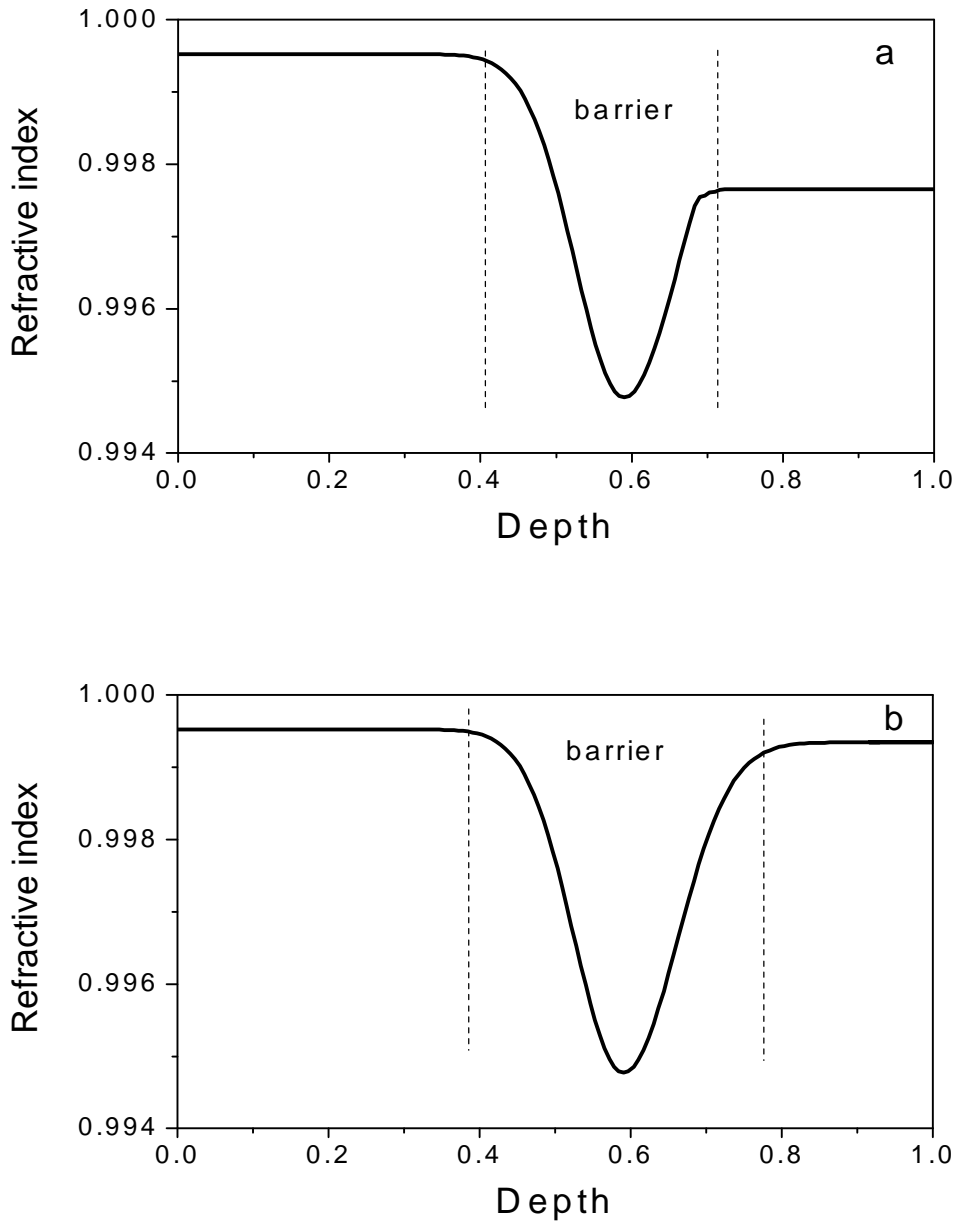


Fig. 2.1.3 (a) barrier confinement and (b) “well + barrier” refractive index distributions (the refractive index and depth have been normalized)

Ion implantation usually creates color centers (optical absorption sites) by electronic damage, and destroys the equilibrium of the original structures by nuclear collisions [1]. Both of them will inevitably increase the waveguide loss, therefore annealing treatment is usually necessary for most ion implanted waveguides. The aim of annealing is to remove the unwanted defects in

waveguides to maximally recover the original properties of substrates. The methods so far include conventional furnace annealing [11], rapid thermal annealing [12] and laser beam processing [13]. Depending on the substrate properties, thermal treatment at 200–500°C are often performed in furnaces for tens of minutes to several hours, which in some cases, may reduce the propagation losses of the waveguides to be as low as in the order of 0.1 dB/cm. Moreover, the rapid thermal annealing may abolish the induced defects while simultaneously avoid unwanted diffusion. Recently, laser beam processing was found to be potentially beneficial [14]. By using strongly absorbed radiation, laser energy may be confined to the surface layer to realize local heating, which may remove intrinsic defects and induce crystalline re-growth or solid phase epitaxy.

2.1.4 Conventional ion implantation and swift-heavy ion implantation

Conventional ion implantation utilizes the energies from several hundreds of keV to several MeV. Light ions (typically refer to H or He) are with energies of 0.3–1MeV and 1–3MeV for H and He respectively. Since the atomic mass of these ions is very small, the implantation usually causes less damage in the waveguide regions; however, in another sense, the ion dose for effective waveguide formation in optical materials is usually high (typically $\sim 10^{16}$ ions/cm²). Some “heavy” ions usually refer to middle-mass ion such as C, N, O, F, Si, Cl, Ni, or Cu. In heavy ion implantation case, the energy loss is much higher than that of light ions. As a result, heavy ions often induce large refractive index variations in optical materials even at low doses 10^{14} ions/cm² with energies of 3–6 MeV [10].

With the advent of newer, more powerful particle accelerators, the effects of swift-heavy ion implantation (SHI) through materials have been explored [4]. Ions with energies greater than 1 MeV/amu can be called “swift” ions. The

main advantages of SHI over conventional ion implantation are its ultralow dose ($\sim 10^{12}$ ions/cm² or even lower) and much higher energy loss. One existing problem for SHI is that such high energy implantation machines are not common at present.

2.2 Light propagation in waveguides

The heart of an optical waveguide is confining light propagation in the waveguide structure. The following aspects of engineering play a role in the study of light propagation in waveguides: (1) the phenomenon of total internal reflection; (2) electromagnetic theory. These two topics are given an introductory review in Sections 2.2.1-2.2.2

2.2.1 Ray optics

Ray optics offers the most basic perspective of light propagation in dielectric waveguides. The location and direction of light is represented by geometrical rays, as shown in figure 2.2.1.

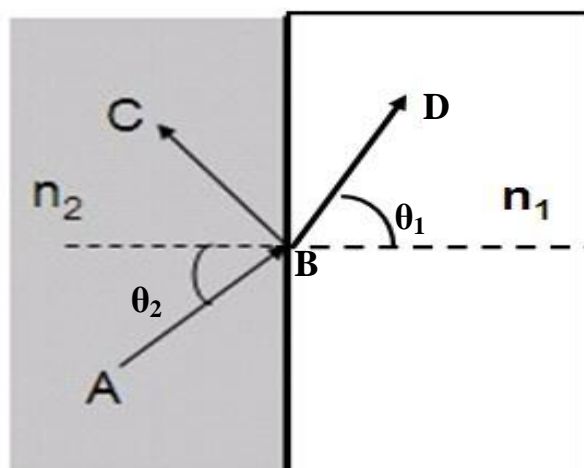


Fig. 2.2.1 Ray optics illustration

Fermat's Principle states that the optical ray traveling between points A and B

follows a path such that the time of travel is a minimum relative to alternate paths [15]. When the ray is incident upon another medium (with refractive index $n_1 < n_2$), the incident ray is split into a reflected ray BC (which remains in the original medium) and a refracted ray BD (which enters the new medium). The geometrical path of the refracted ray obeys Snell's Law: $n_1 \sin \theta_1 = n_2 \sin \theta_2$. When θ_2 reaches a critical angle such that $\theta_1 = 90$ degrees, the refracted ray BD lies along the interface between the two media. Beyond the critical angle, θ_1 is imaginary and the incident ray is totally reflected, thus remaining within the original medium. This concept of total internal reflection is the basis for confining light within a desired medium and creating an optical waveguide [16].

2.2.2 Waveguide configuration

A channel waveguide (with guidance in both directions) has a guiding structure in the form of a stripe with a finite width. This may be a ridge on top of the cladding structure or an embedded channel. The latter has more symmetric waveguide modes. Channel waveguides are extensively used, for example, within various laser diodes.

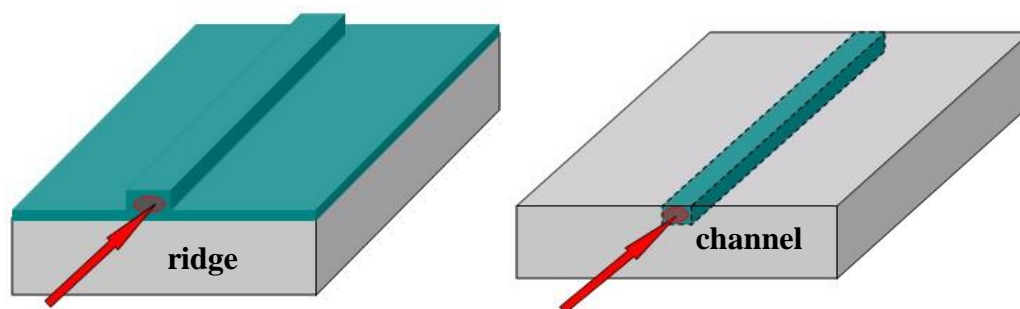


Fig. 2.2.2 Structure of rid and channel waveguides

When a thin layer with a slightly increased refractive index is fabricated on top of some crystal or glass, it functions as a planar waveguide. Light injected into the waveguide layer with a small enough divergence will be guided

perpendicular to the layer and unguided in the other direction. The waveguide layer embedded between two cladding layers is called buried waveguide. Planar optical waveguide are key elements in the modern, high speed optical network. In this work, we will focus on ion implanted planar waveguides.

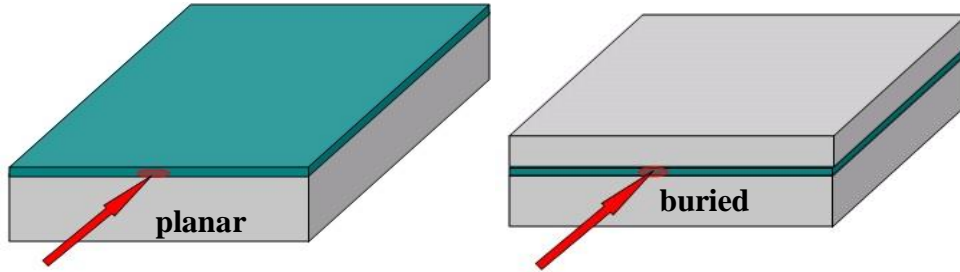


Fig. 2.2.3 Structure of planar and buried waveguide

2.2.3 Electromagnetic analysis of a planar waveguide

For the purpose of developing a model for light propagation in an optical waveguide, electromagnetic wave theory must be considered. For a dielectric medium, the electromagnetic fields satisfy the following well-known Maxwell equations:

$$\nabla \times \vec{E} = -\frac{\partial \vec{B}}{\partial t} \quad (1)$$

$$\nabla \times \vec{H} = \frac{\partial \vec{D}}{\partial t} \quad (2)$$

$$\nabla \times \vec{D} = 0 \quad (3)$$

$$\nabla \times \vec{B} = 0 \quad (4)$$

where \vec{E} is the electric field, \vec{B} magnetic flux density, \vec{H} magnetic field and \vec{D} is electric flux density. The four vector fields have relations as follows:

$$\vec{D} = \epsilon \vec{E} \quad (5)$$

$$\vec{B} = \mu \vec{H} \quad (6)$$

where ϵ is the dielectric permittivity and μ is the magnetic permeability of the

medium.

Combining (1) - (6) and using the divergence condition $\nabla \times (\nabla \times \vec{Y}) = \nabla(\nabla \cdot \vec{Y}) - \nabla^2(\vec{Y})$ we can obtain the wave equations:

$$\nabla^2(\vec{E}) = me \frac{\partial^2 \vec{E}}{\partial t^2} \quad (7)$$

$$\nabla^2(\vec{H}) = me \frac{\partial^2 \vec{H}}{\partial t^2} \quad (8)$$

In waveguides, electrical and magnetic fields are functions of the spatial \vec{r} and time t . For monochromatic waves, the solutions of (7) and (8) have the form

$$\vec{E}(\vec{r}, t) = \vec{E}(\vec{r}) \exp(j\omega t) \quad (9)$$

$$\vec{H}(\vec{r}, t) = \vec{H}(\vec{r}) \exp(j\omega t) \quad (10)$$

Substituting (9) and (10) into (7) and (8) respectively, we can obtain

$$\nabla^2(\vec{E}) + k^2 \vec{E} = 0 \quad (11)$$

$$\nabla^2(\vec{H}) + k^2 \vec{H} = 0 \quad (12)$$

where k is the wave number, given by

$$k = k_0 n = k_0 \sqrt{\epsilon_r} = \omega \sqrt{\epsilon_0 \epsilon_r \mu_0} = \omega \sqrt{\epsilon \mu_0} \quad (13)$$

In equation (13), k_0 is the wave number in a vacuum, n is the refractive index of the medium, ϵ_r is the relative permittivity of the material which is constant in the medium, ω the angular frequency of the electromagnetic field and ϵ_0 and μ_0 are the permittivity and permeability of a vacuum. (11) and (12) are the reduced wave equations, called Helmholtz equations.

At most cases, a planar waveguide is uniform in the z direction (Fig. 2.2.4) and the derivation of an electromagnetic field with respect to z coordinate is constant such that [17]

$$\frac{\partial}{\partial z} = -j\beta \quad (14)$$

where β is the propagation constant and is the z-directed component of the wave number k . The ratio of the propagation constant in the medium to the wave number in a vacuum is called the effective index:

$$n_{eff} = \frac{\beta}{k_0} \quad (15)$$

Thus, we can summarize the Helmholtz equations as

$$\frac{\partial^2 \vec{E}}{\partial x^2} + \frac{\partial^2 \vec{E}}{\partial y^2} + (k^2 - \beta^2) \vec{E} = 0 \quad (16)$$

$$\frac{\partial^2 \vec{H}}{\partial x^2} + \frac{\partial^2 \vec{H}}{\partial y^2} + (k^2 - \beta^2) \vec{H} = 0 \quad (17)$$

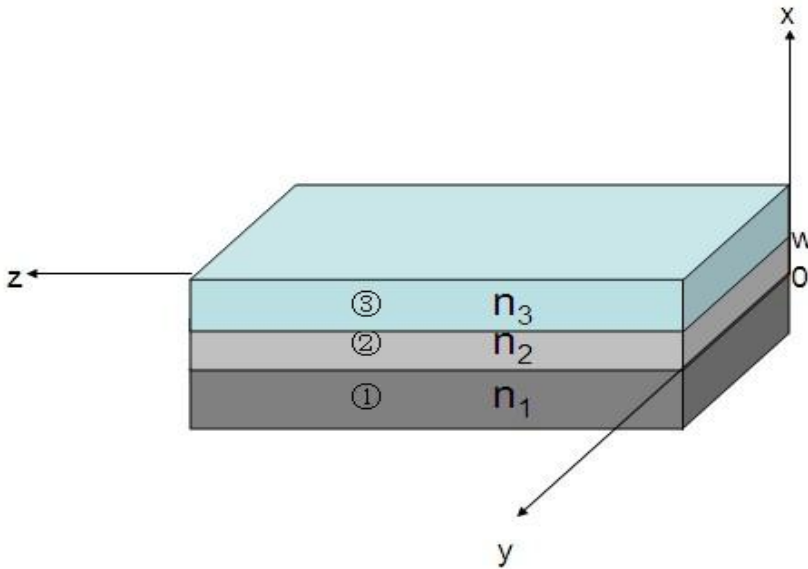


Fig. 2.2.4 Three-layer planar waveguide

For simplicity, we pay attention to a three-layer planar waveguide as shown in Fig. 2.2.4. The waveguide is uniform in the y and z directions. Region 1 and 3 are cladding layers, and region 2 is a guiding layer. Since the structure is uniform in the y direction, we can assume the second term in (16) and (17) is zero.

Next, we discuss the two modes that propagate in the waveguide: the transverse electric mode (TE mode) and the transverse magnetic mode (TM mode). In the TE mode, the electric field is only in the y direction and the magnetic field is in the x and z direction [17]. As a result, we get the following wave equation from (16):

$$\frac{d^2 E_y}{dx^2} + k_0 (n_2^2 - n_{eff}^2) E_y = 0 \quad (18)$$

In the TM mode, the magnetic field is only in the y direction and the electric field is in the x and z direction. From equation (17), we can get:

$$\frac{d^2 H_y}{dx^2} + k_0 (n_2^2 - n_{eff}^2) H_y = 0 \quad (19)$$

Equations (18) and (19) are the basis of analyzing planar waveguides and will be used in the Reflectivity Calculation Method in next chapter.

2.3 Thermal-spike model

The application of the thermal-spike model to irradiation phenomena in crystals is an old idea [18]. The basic assumption of all thermal-spike models is that a high-temperature region around the trajectory of a high-energy ion is formed in the material. In the following, a melt is formed when the temperature exceeds the melting point of the crystal and the melted crystal becomes amorphous. F. Agulló-López et al. extend the thermal-spike model to discuss preamorphization stages in crystals, i.e., the generation of preamorphized regions during ion irradiation [19]. In this section, F. Agulló-López's model, whose accuracy has been verified for swift-heavy ion implanted LiNbO₃, will be introduced.

The implanted ion transfers an electronic energy loss S_e per unit length to the substrate. This energy is then passed onto the ionic lattice with a certain efficiency factor $g < 1$ independent of S_e . The transferred energy generates a

certain temperature distribution $\Delta T(r, t, S_e)$. Here, r is the distance from the ion and t is time. At $t=0$ we assume a Gaussian distribution:

$$\Delta T(r, 0, S_e) = \frac{Q}{2\rho a_0^2 r C} e^{-r^2/2a_0^2} \quad (20)$$

where a_0 is the width of the initial Gaussian distribution, ρ the crystal density, C the specific heat, $\Delta T=T-T_s$, T_s being the substrate temperature and $Q=gS_e$ the energy per unit length transferred to the ionic lattice. Then, the model uses the following assumptions:

- (1) The area under the Gaussian is preserved. This condition requires that heat conduction is the only heat transport mechanism, i.e., radiation is neglected.
- (2) The mechanical and thermal parameters do not depend on temperature, which is a reasonable assumption at high temperatures (near the melting point).
- (3) The heat conduction in the direction perpendicular to the input surface is ignored so that at every depth the transport processes are two dimensional.

From these assumptions $\Delta T(r, t, S_e)$ can be obtained for $t>0$ arbitrarily [20]:

$$\Delta T(r, S_e) = \frac{Q}{2\rho a_0^2 r C} e^{-r^2/2a_0^2} \quad 0 < r < \sqrt{2} a_0 \quad (21)$$

$$\Delta T(r, S_e) = \frac{Q}{\rho e r C} \frac{1}{r^2} \quad r > \sqrt{2} a_0 \quad (22)$$

The maximum of those temperatures is attained at $r=0$:

$$\Delta T_{\max}(0, S_e) = \frac{Q}{2\rho a_0^2 r C} \quad (23)$$

Assuming T_m being the melting temperature of the crystal, the critical required stopping power S_m is obtained through

$$T_m = \frac{gS_m}{2\rho a_0^2 r C} \quad (24)$$

The concentration of intrinsic defects generated by the swift ion and responsible for the structural damage is given by some effective Arrhenius law

[21],

$$c(T) = Ae^{-\varepsilon/kT} \quad (25)$$

Then, ε is the formation energy of the responsible defect, k the gas constant and A a factor related to the formation entropy s of the defect, $A=e^{s/k}$.

In order to determine the lattice structure around the ion trajectory one should define a certain critical defect concentration to initiate the melted and subsequently amorphous phase (core) as well as to characterize the damaged or preamorphized regions (tail) around the core (Fig. 2.3.1). In many crystals the critical melting concentration c_m , derived from a comparison to experimental data [22], is roughly around 10^{-3} (normalized to atomic concentration). As to the so-called preamorphized regions (tail), one may safely consider that they should contain a defect concentration $c_h / c_m \geq 10^{-3}$, i.e., c_h over 10^{-6} , which represents some typical background concentration of defects. Anyhow, the particular values assumed for these concentrations, c_m and c_h , are a matter of convention and do not enter directly in any of the predictions of the model.

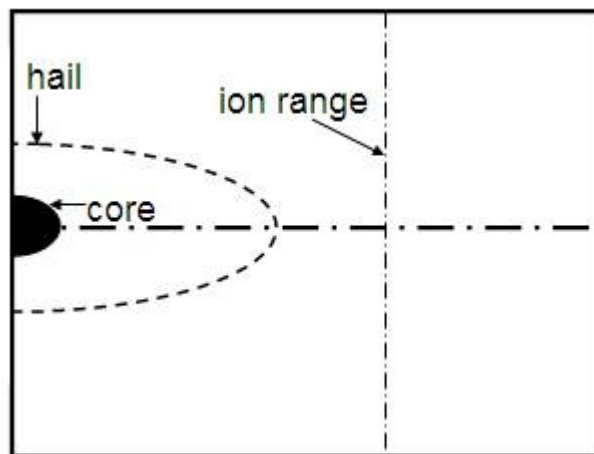


Fig. 2.3.1 Structure of the core, halo, and tail [19]

The preamorphized areas play an important role in the stages of damage, i.e., on the memory effect. This situation is well accepted for nuclear damage that is assumed to be permanent or accumulative. However, the situation has not been addressed for the case of the electronic damage, in spite of the extensive effort

devoted to investigating the physical basis and finding technological applications for latent tracks. Let us consider an ion beam with energy E having an electronic stopping power S_e at a given depth z in the crystal. In this section we will refer, as a particular case, to $z=0$, i.e., to the input surface of the crystal. In the case of $S_e < S_m$, the maximum local concentration of defects generated is $c < c_m$. Therefore, latent tracks are not produced since electronic energy losses are below threshold. However, during irradiation intrinsic lattice defects will be introduced, facilitating the eventual achievement of threshold conditions for the next ions moving through the damaged areas.

After a fluence φ an average defect concentration $c(\varphi, S_e)$ has been produced. If $c \geq c_m$ the crystal is already amorphized. Let us consider the case of $c < c_m$. The additional defect concentration c must introduce in order to reach the threshold value for amorphization c_m and $c = c_m - c(\varphi, S_e)$. From (25), the temperature that should be reached to generate that additional defect concentration and so to melting of the previously damaged crystal is

$$T_{\max,th} = \frac{T_m}{1 - \frac{kT_m}{e} \log_e \left(1 - \frac{c}{c_m}\right)} \quad (26)$$

The function $c(\varphi, S_e)$ can be readily calculated as

$$c(\mathbf{j}, S_e) = \frac{N}{A} \iint_A c[\Delta T(r, S_e)] dx dy \quad (27)$$

where x and y are the Cartesian coordinates at the surface, A the area of the irradiated region, and N the total number of incident particles. Noticing that the fluence is just $\varphi = N/A$ and that the integrand is nonzero in a very small region as compared to the macroscopic domain A , the limits of the integral can be extended to infinity. Transforming to polar coordinates one obtains:

$$\bar{c}(\mathbf{j}, S_e) = 2pj \int_0^{\infty} rc[\Delta T(r, S_e)] dr \quad (28)$$

This integral uses expressions (21), (22) and (25). It has to be divided into two

summands, according to the piecewise definition (21) and (22). The result of the calculation (require some algebra) is:

$$\frac{c(j, S_e)}{c_m} = 2pj a_0 \left\{ \int_1^e \frac{1}{u} \exp\left[-\frac{e}{kT_m} \left(\frac{S_m}{S_e} u - 1\right)\right] du + \frac{1}{e} \frac{kT_m}{e} \frac{S_e}{S_m} \exp\left[-\frac{e}{kT_m} \left(\frac{S_m}{S_e} e - 1\right)\right] \right\} \quad (29)$$

The thermal-spike model above will be applied on swift-heavy ion implanted Nd:YAG waveguides in chapter 5.

2.4 Chalcogenide glass and Nd:YAG crystal

2.4.1 Gallium lanthanum sulphide (GLS) glass

The glass forming ability of gallium sulphide and lanthanum sulphide was discovered in 1976 by Loireau-Lozac'h et al [23]. GLS glasses have a wide region of glass formation centered about the $70\text{Ga}_2\text{S}_3 : 30\text{La}_2\text{S}_3$ composition (molar ratio) and can readily accept other modifiers into their structure [24]. This means that GLS can be compositionally adjusted to give a wide variety of optical and physical responses. For example, the addition of CsCl increases the thermal stability region of GLS [25] and the addition of La_2F_6 improves thermal stability, increases visible transmission and decreases OH impurity levels [26]. It is necessary to add a small percentage, typically 2% by weight, of lanthanum oxide to form a glass. Without this oxide, crystallization of the glass is a problem and glass formation is hindered [27]. GLS has a high refractive index of ~ 2.4 , a transmission window of $\sim 0.5\text{-}10\mu\text{m}$ and a low maximum phonon energy of $\sim 425\text{ cm}^{-1}$ [28]. Table I summarizes some of the properties of GLS glass.

Table I Properties of GLS glass

Refractive index at 0.633 μm	Nonlinear index ($\times 10^{-20} \text{ m}^2\text{W}^{-1}$) at 1.55 μm	Bulk transmission at 50% (μm) through 1 cm	Glass transition ($^{\circ}\text{C}$)	Density (g/cm^3)
2.446	216	0.5-10	580	4.04

It appears that the common chalcogenide glasses suffer from poor rare-earth solubility (e.g. As_2S_3) [29] or low glass transition temperature (e.g. As_2Se_3) [30], both of which cause the scarcity of waveguide lasers in chalcogenide glass. So far, gallium lanthanum sulfide (GLS) glass seems to be the only one glass well-suited for use in active waveguides. Its high glass transition temperature ($T_g=580^{\circ}\text{C}$) makes GLS appropriate for application in high temperature. High rare earth dopant concentrations without clustering are possible owing to the fact that the rare earth ions substitute for the lanthanum ions in the glass matrix [31]. However, GLS glasses have a high dn/dT (n refractive index and T temperature) and low thermal conductivity, causing strong thermal lensing, thus they are not suitable for bulk lasers. As a result, waveguide structure in GLS is the only choice to realize lasers or amplifiers which have been realized in Nd and Er doped GLS glass, respectively [32, 33]. Other active area of research into GLS include its acousto-optics properties, IR lens moulding, $2\mu\text{m}$ Er:YAG laser power delivery for dentistry applications, nonlinear micro resonators and electrical and optical data storage utilizing the change in resistivity and reflectance of GLS in its crystalline and vitreous phase respectively [34].

2.4.2 Metal elements doped GLS glass

Metal elements doped lasers and amplifiers have found application in a

number of different areas including telecommunication, material processing, medical diagnosis and treatment, printing and marking, environmental sensing, counter measures, etc. The doping metal elements are divided into rare-earth and transition metal dopants. In this work, we pay attention to holmium (Ho), neodymium (Nd) and titanium (Ti).

Ho^{3+} is commonly known for its 2 μm transition in crystal lasers for coherent laser radar and medical applications [35]. Due to the rapidly developing application fields in atmospheric sensing, optical radar (collision avoiding radar), remote control, etc, mid-infrared (MI) light sources are strongly demanded. However, the report on rare-earth doped glass waveguides which can be used as MI waveguide lasers is less well known. The lower phonon energy GLS glass offers the possibility for lasers at 3.9 and 4.9 μm [36]. The first wavelength is of particular interest for the long-wave project because it coincides with the attenuation minimum of the 3.4-4.1 μm atmospheric transmission window. Fig. 2.4.1 shows the atmospheric transmission from 0.1 to 100 μm . The window is determined by the H_2O and CH_4 absorption bands on the short-wavelength side and the CO_2 absorption on the long-wavelength side. The 4.9 μm overlaps with the fundamental absorption of carbon monoxide, making the glass a potential waveguide laser source for gas sensing applications.

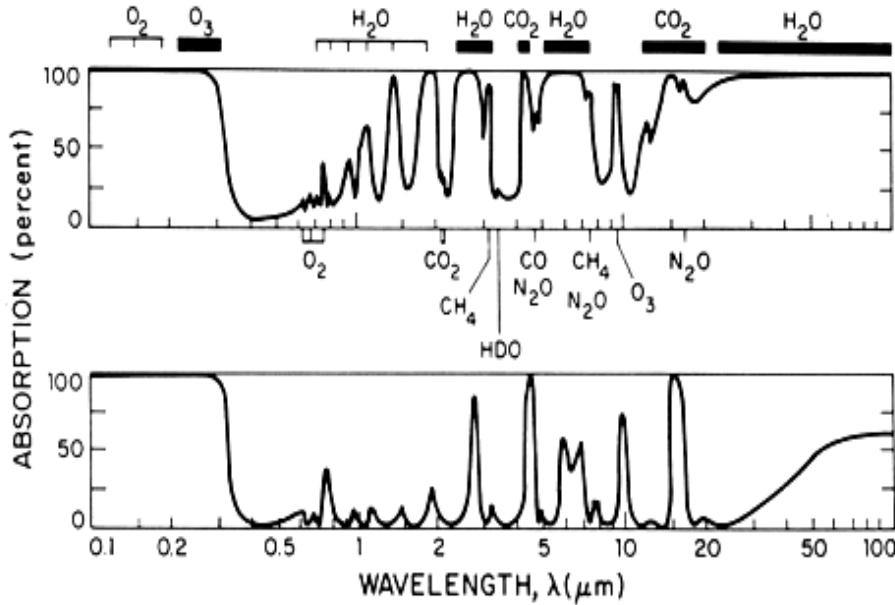


Fig. 2.4.1 Absorption spectra of solar radiation reaching the earth's surface (top) and reaching an altitude of 11km (bottom) [37].

As we know, certain transparent materials with a small concentration of Nd^{3+} ions can be used in lasers as gain media for infrared wavelengths (1054–1064 nm), e.g. Nd:YLF (yttrium lithium fluoride), Nd:YVO₄ (yttrium orthovanadate), and Nd:glass. The Nd^{3+} ion has not been studied widely as a dopant for chalcogenide glasses because the main fluorescent energy level ($^4\text{F}_{3/2}$) has a large gap to the next lower lying level and hence does not suffer from competing non-radiative multi-phonon decay. Among the few works, Nd:GLS glass is the most extensively studied system and the only system with reported laser action (1.08 μm) in bulk and fiber form [37].

Ti doped Al_2O_3 (Ti:Sapphire) has been used as a gain medium in tunable lasers since laser action was first reported by Moulton in 1982 [38]. The Ti:Sapphire laser is the most widely used near infrared tunable laser source and is tunable from 650 to 1100nm, it is also used to generate ultra short laser pulses with durations as low as 8fs [39]. Because of the success of the Ti:Sapphire crystal as a tunable laser source little attention has been paid to titanium doped glass as an active medium and reports in the literature of

photoluminescence from titanium doped glasses are extremely scarce. A titanium doped glass laser in a waveguide geometry could potentially have several advantages over a Ti:Sapphire laser in that it could be more compact, have a higher alignment stability and robustness. The high maximum phonon energy and resulting rapid non-radiative decay mechanisms of oxide-based glasses such as silica make conventional glasses unlikely candidates for the host material. The low maximum phonon energy of GLS glass may allow emission from transition metal dopants that are weakly or not at all observed in oxide-based glasses. Figure 2.4.2 exhibits the photoluminescence spectra of 0.1% Ti doped GLS and GLSO glass. The 800-1700nm broad luminescence band shows the potential of Ti:GLS (GLSO) as new non-crystalline tunable solid state laser sources

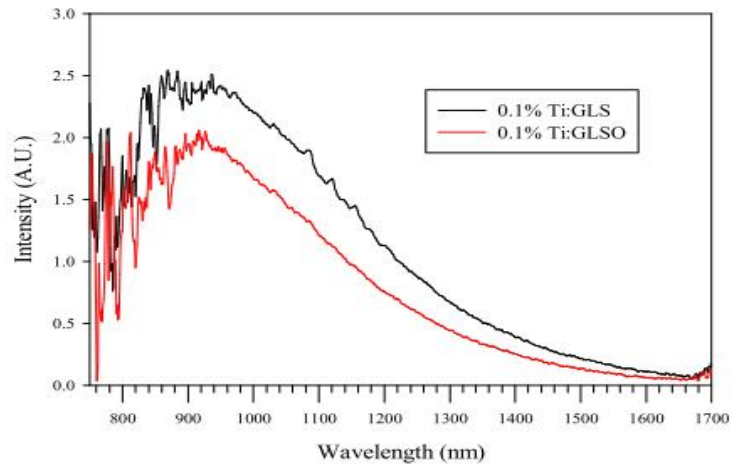


Fig. 2.4.2 Photoluminescence spectra of 0.1% titanium-doped GLS (molar ratio, $65\text{Ga}_2\text{S}_3:29.9\text{La}_2\text{S}_3:5\text{La}_2\text{O}_3$) and GLSO ($74.9\text{Ga}_2\text{S}_3:25\text{La}_2\text{O}_3$) excited with a 5mW 633nm laser source [40]

2.4.3 Nd:YAG crystal

Nd:YAG (neodymium-doped yttrium aluminum garnet; $\text{Y}_3\text{Al}_5\text{O}_{12}$) is an extensively used laser crystal. Generally the crystalline host is doped with around 1% neodymium by atomic percent. Up to now, almost all the

high-power lasers use this crystal as their working medium.

Nd:YAG can offer substantial laser gain even for moderate excitation levels and pump intensities. The gain bandwidth is relatively small, but this allows for a high gain efficiency and thus low threshold pump power. The most common Nd:YAG emission wavelength is 1064nm. Starting with that wavelength, outputs at 532, 355 and 266nm can be generated by frequency doubling, frequency tripling and frequency quadrupling, respectively. Other emission lines are at 946, 1123, 1319, 1338 and 1444nm. Energy level structure and common pump (blue line) and laser transitions (red line) of the trivalent neodymium ion in Nd:YAG are shown in Fig. 2.4.3.

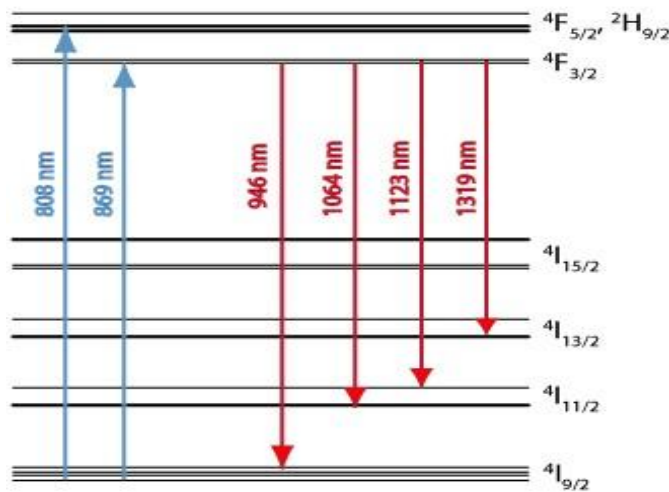


Fig. 2.4.3 Energy level and pump/transition wavelength of Nd:YAG

References

1. P. D. Townsend, *J. Phys. E* 10, 197 (1977).
2. D. Wei, W. Lee and L. Bloom, *Appl. Phys. Lett.* 22(1), 5 (1973)
3. F. Qiu and T. Narusawa, *Jpn. J. Appl. Phys.* 49, 092503 (2010).
4. P. D. Townsend, P.J. Chandler, and L. Zhang, *Optical Effects of Ion Implantation*, Cambridge University Press, Cambridge, 1994.
5. N. Bohr, *Mat. Fys. Medd. Dan. Vid. Selsk* 18 (8), 1 (1948).
6. J. Lindhard, M. Scharff and H. Schiott, *Mat. Fys. Medd. Dan. Vid. Selsk* 33 (14), (1963).
7. J. F. Ziegler, computer code, SRIM <http://www.srim.org>.
8. P. J. Chandler, L. Zhang and P. D. Townsend, *Solid State Phenom* 27, 129 (1992).
9. F. Qiu and T. Narusawa, *Opt. Mater.* 33, 527 (2011).
10. F. Chen, *J. Appl. Phys.* 106(8), 081101 (2009).
11. A. Gumennik, A.J. Agranat, I. Shachar and M. Hass, *Appl. Phys. Lett.* 87, 251917 (2005).
12. M. Feuster, Ch. Buchal, E. Sneoks and A. Polman, *Appl. Phys. Lett.* 65, 225 (1994).
13. P. D. Townsend and J. Olivares, *Appl. Surf. Sci.* 109/110, 275 (1997).
14. P. D. Townsend, *Vacuum* 51, 301 (1998).
15. B. Saleh and M. Teich, *Photonics*, J. Wiley & Sons, 1991.
16. D. Marcuse, *Theory of Dielectric Optical Waveguides*, Academic Press, 1974.
17. K. Kawano and T. Kitoh, *Introduction To Optical Waveguide Analysis*, John Wiley and Sons, Inc., 2001.
18. F. Seitz and J. F. Koehler, *Solid State Physics: Advances in Research and Applications*, Academic, New York, 1956.

- 19.F. Agulló-López, G. García, and J. Olivares, *J. Appl. Phys.* 97, 093514 (2005).
- 20.G. Szenes, *Mater. Sci. Forum* 97-99, 647 (1992).
- 21.F. Agulló-López, C. R. A. Catlow and P. D. Townsend, *Point Defects in Materials Academic*, London, 1988.
- 22.J. Frenkel, *Kinetic Theory of Liquids*, Dover, New York, 1955.
- 23.A. M. Loireau-Lozac'h, M. Guittard and J. Flahaut, *Mater. Res. Bull.* 11, 1489 (1976).
- 24.M. N. Petrovich, PhD Thesis, University of Southampton, 2003.
- 25.A.Y. Ramos, M.G. Cardona, H.C.N. Tolentino, M.C.M. Alves, N. Watanabe, O.L. Alves and L.C. Barbosa, *J. MATER. RES.* 16(5), 1349 (2001).
- 26.S.P. Morgan, D. Furniss and A.B. Seddon, *J. NON-CRYST. SOLIDS.* 203, 135 (1996).
- 27.T. Schweizer, F. Goutaland, E. Martins, D.W. Hewak and W.S. Brocklesby, *J. Opt. Soc. Am. B* 18(10), 1436, (2001).
- 28.A. Mairaj, PhD Thesis, University of Southampton, 2002.
- 29.A. Zakery, S.R. Elliott, *J. Non-Crystal. Solids* 330, 1 (2003).
- 30.R. G. Decorby, N. Ponnampalam, M. H. Pai, H. T. Nguyen, P. K. Dwivedi, T. J. Clement, C. J. Haugen, J. N. McMullin and S. O. Kasap, *IEEE J. Sel. Top. Quantum Electron.* 11, 539 (2005).
- 31.D. W. Hewak, R. C. Moore, T. Schweizer, J. Wang, B. Samson, W. S. Brocklesby, D. N. Payne and E. J. Tarbox, *Electronics Lett.* 32, 384(1996).
- 32.A. K. Mairaj, C. Riziotis, A. M. Chardon, P. G. R. Smith, D. P. Shepherd and D. W. Hewak, *Appl. Phys. Lett.* 81, 3708 (2002).
- 33.J. A. Frantz, L. B. Shaw, J. S. Sanghera and I. D. Aggarwal, *Opt. Express* 14, 1797 (2006).
- 34.M. A. Hughes, PhD Thesis, University of Southampton, 2007.

35. T. Y. Fan, G. Huber, R. L. Byer and P. Mitzscherlich, *IEEE J. Quantum Electron.* 24, 924 (1988).
36. J. Schneider, *Electron. Lett.* 31, 1250 (1995).
37. T. Schweizer, PhD Thesis, Optoelectronics Research Centre, University of Southampton and Institut für Laser-Physik, Universität Hamburg.
38. P.F. Moulton, *J. Opt Soc. Am. B* 3(1), 125 (1986).
39. A. Stingl, M. Lenzner, C. Spielmann and F. Krausz, *Opt. Lett.* 20 (6), 604 (1994).
40. M. A. Hughes, R. J. Curry and D. W. Hewak, *J. Opt. Soc. Am. B* 25 (9), 1458 (2008).

Chapter 3 Experimental methods

In this chapter, the prism coupling technique, reflectivity calculation method for reconstructing refractive index profiles, end-fire coupling method, back-reflection method for measuring propagation loss, Fourier transform infrared spectroscopy and Raman spectroscopy are described.

3.1 Prism coupling

The use of prism coupling for excitation of waveguide modes in planar waveguides was first studied by Tien et al [1]. Since then, prism coupling has become an important technique in integrated optics. Figure 3.1.1 shows the scheme of prism coupling.

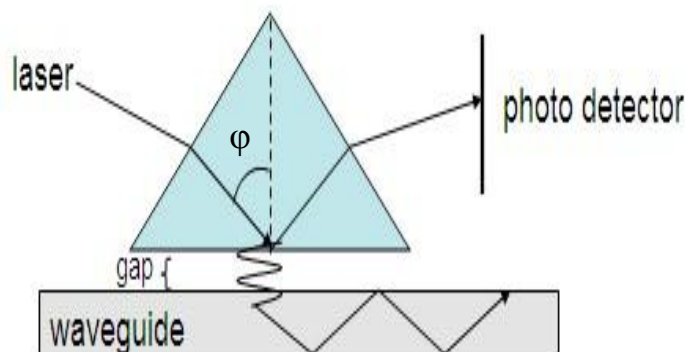


Fig. 3.1.1 Scheme of prism coupling.

A prism with higher refractive index than the waveguide is pressed against it, leaving a small air gap between the base of the prism and the top of the waveguide. This gap must be of the order of $0.1\mu\text{m}$ for allowing the evanescent fields [2] of the entering light beam to couple into the waveguide. A laser beam enters the prism and is totally reflected at its base. The total reflection leaves only evanescent fields in the air gap, and it is these evanescent fields which couple the light wave from the prism into the waveguide.

One mode can be excited in the waveguide when the equation (1) is satisfied.

$$N_m = n_p \sin \phi \quad (\text{m is the number of mode}) \quad (1)$$

In equation (1), N_m is the effective refractive index of the mode in the waveguide, n_p is the refractive index of the prism, ϕ is the angle as shown in Fig. 3.1.1. As a result, successive modes can be excited in the waveguide by orienting the angle ϕ . When one mode is excited in the waveguide, some light propagates in the waveguide and thus less light is detected by the photo detector. The phenomenon that less light is projected on the photo detector (resulting in a low intensity peak) is called dark modes.

3.2 Reflectivity calculation method

Reflectivity calculation method (RCM) developed by Chandler and Lama [3] has demonstrated the ability of reconstructing the refractive index profiles of ion implanted waveguides remarkably well [4]. RCM attempts to model the refractive index profiles according to the observed dark modes. In fact, dark modes can be seen as an interference effect produced by the reflectivity of light at single point on the coupling prism interface. If resonance occurs at a certain coupling angle, more light will be absorbed than at non-resonance, and so less light will be reflected back on to the detector.

Figure 3.2.1 gives a mode of refractive index profile of a typical ion implanted waveguide [4]. The transverse light component is considered in the positive x direction from the prism into the guide, and then leak into the substrate through the barrier. Because of partial reflections at all the step boundaries, there is also a travelling wave in the negative x direction. These two opposite travelling waves can be represented as $\exp i(\pm k_x x - \omega t)$. Here, k_x is the x component of the wave vector in the medium and is written as

$$k_x = k_0 [n^2(x) - n_{eff}^2]^{\frac{1}{2}} \quad (1)$$

k_0 is the wave number in a vacuum, and n_{eff} the effective refractive index. It is necessary to emphasize that n_{eff} is no longer an eigenvalue of a waveguide mode, but is continuously variable. A and B represent the amplitudes of the two opposite travelling waves in any region (as shown in Fig. 3.2.1). According to the equation (18) in last chapter, the general wave function in the x direction can be written as

$$E(x) = A \exp(ik_x x) + B \exp(-ik_x x) \quad (2)$$

k_x can be either real, representing an oscillating wave, or imaginary representing an evanescent wave. In the former case, E(x) can be rewritten as

$$E(x) = A \cos(k_x x) + B \sin(k_x x) \quad (3)$$

where $k_x = k_0 [n^2(x) - n_{\text{eff}}^2]^{\frac{1}{2}}$, and in the latter case E can be rewritten as

$$E(x) = A' \exp(k'_x x) + B' \exp(-k'_x x) \quad (4)$$

where $k'_x = k_0 [n_{\text{eff}}^2 - n^2(x)]^{\frac{1}{2}}$. As shown in Fig. 3.2.1, the whole system is divided into five layers, prism, air, guide, barrier and substrate. The two amplitudes A and B (A' and B') are related to those in an adjacent region by the two boundary condition requirements. At the j and j+1 boundary, these are

$$H_j(x) = H_{j+1}(x) \quad (5a)$$

$$E_j(x) = E_{j+1}(x) \quad (5b)$$

For the TE mode, (5a) can be rewritten as

$$\frac{\partial E_j(x)}{\partial x} = \frac{\partial E_{j+1}(x)}{\partial x} \quad (6a)$$

and for TM mode (5b) can be rewritten as

$$\frac{1}{n_j^2} \frac{\partial H_j(x)}{\partial x} = \frac{1}{n_{j+1}^2} \frac{\partial H_{j+1}(x)}{\partial x} \quad (6b)$$

$$\begin{bmatrix} A_j' \\ B_j' \end{bmatrix} = \begin{bmatrix} \frac{\exp(k'_{xj} T_j)}{2} & -\frac{k'_{x(j+1)} \exp(k'_{xj} T_j)}{k'_{xj} 2} \\ 1 & \frac{k'_{x(j+1)}}{k'_{xj}} \frac{1}{2\exp(k'_{xj} T_j)} \end{bmatrix} \begin{bmatrix} A_{j+1} \\ B_{j+1} \end{bmatrix} \quad (9)$$

(4) Oscillating to evanescent (from prism to air, or from guide to barrier).

Then we get

$$\begin{bmatrix} A_j \\ B_j \end{bmatrix} = \begin{bmatrix} \cos(k_{xj} T_j) + \frac{k_{x(j+1)} \sin(k_{xj} T_j)}{k_{xj}} & \cos(k_{xj} T_j) - \frac{k_{x(j+1)} \sin(k_{xj} T_j)}{k_{xj}} \\ \sin(k_{xj} T_j) - \frac{k_{x(j+1)} \cos(k_{xj} T_j)}{k_{xj}} & \sin(k_{xj} T_j) + \frac{k_{x(j+1)} \cos(k_{xj} T_j)}{k_{xj}} \end{bmatrix} \begin{bmatrix} A'_{j+1} \\ B'_{j+1} \end{bmatrix} \quad (10)$$

The incident and reflected light at the prism (A_1 and B_1 in Fig. 3.2.1) may therefore be related to the two amplitudes in the substrate (A_s and B_s) by the product of the above 2×2 matrices (from (7) to (10)). Thus, we can get

$$\begin{bmatrix} A_1 \\ B_1 \end{bmatrix} = \begin{bmatrix} P_{11} & P_{12} \\ P_{21} & P_{22} \end{bmatrix} \begin{bmatrix} A_s \\ B_s \end{bmatrix} \quad (11)$$

Since the substrate is much thicker than the waveguide, there is no light travelling back from the substrate, i.e. $B_s=0$. Hence the reflection from the prism interface is given by

$$R = \left| \frac{B_1}{A_1} \right|^2 = \left| \frac{P_{21}}{P_{11}} \right|^2 \quad (12)$$

For TM mode, the method is the same but just multiply (k_{j+1}/k_j) by $(n_j/n_{j+1})^2$ or (k'_{j+1}/k'_j) by $(n'_j/n'_{j+1})^2$.

Then the refractive index distribution of an ion implanted waveguide can be determined by the following steps:

- (1) Choose an analytic function for the index profile characterized by several parameters;
- (2) Continuously change the effective refractive index n_{eff} and then calculate the reflectivity R (equation (12)) of this hypothetical profile by using RCM described above;
- (3) Compare the theoretical mode indices with the experimental values

obtained from prism coupling measurements;

- (4) Keep changing the parameters to alter the index profile shape until the theoretical mode indices match the experimental ones well enough.

3.3 End-fire coupling system

Optical waveguides have a typical cross-section of only a few square microns. In order to efficiently couple light into and out of such a small area a precisely aligned optical system is required.

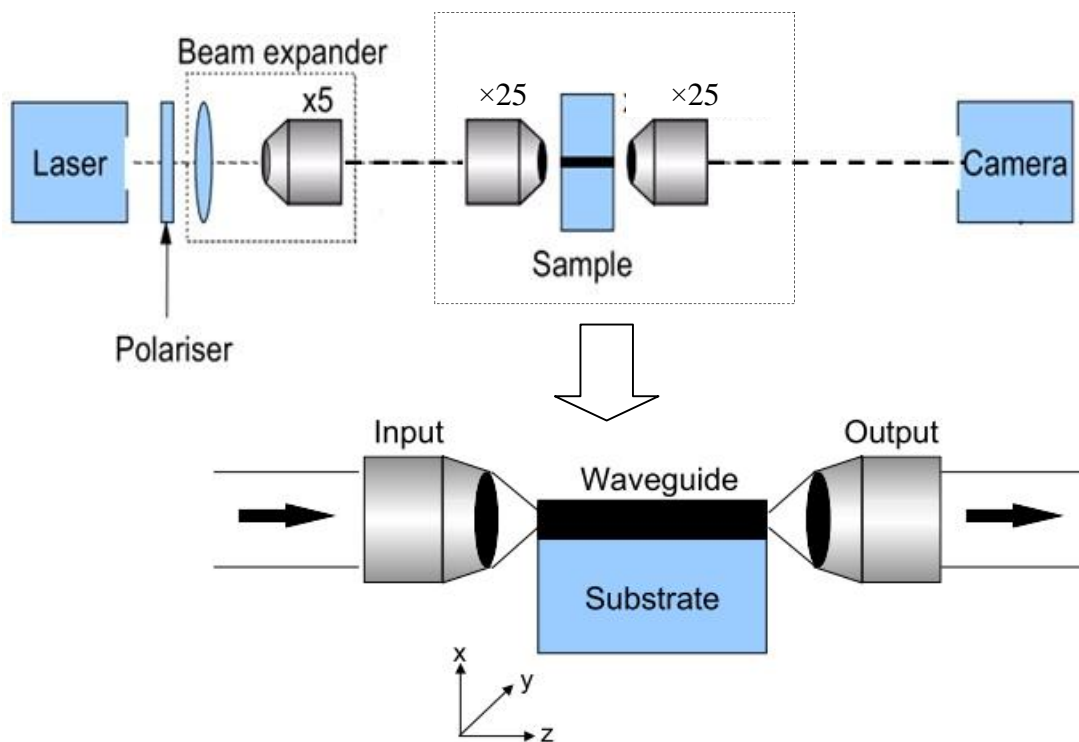


Fig. 3.3.1 End-fire coupling system

An end-fire coupling system is shown schematically in Fig. 3.3.1. The sample to be tested is mounted on a six-dimensional xyz moving optical stage. The stage and sample are then positioned between the two microscope objective lenses such that the end facets of the sample are perpendicular to the optical path. Guided modes of the waveguide are then excited by the input light and the near-field patterns (output light) are collected by the camera.

To maximize the coupling efficiency of the light into a guided mode, it is preferable that the field profile of the exciting beam closely matches that of the fundamental mode of the waveguide. The beam sizes of the lasers used to test waveguides in the present work is larger than that of the guided modes of the waveguides. It is therefore necessary to reduce the spot size by focusing it onto the waveguide through a $\times 25$ microscope objective lens mounted on a xyz moving stage. The minimum obtainable spot diameter D through the microscope objective lens can be calculated by

$$D = \frac{1.54\lambda}{NA} \quad (13)$$

where λ is the wavelength of the light and NA is the numeral aperture of the lens. The $\times 25$ lens used in this work has a NA of 0.65 which gives a minimum spot diameter of $1.5\mu\text{m}$ at a wavelength of 632.8nm .

The minimum spot is obtained when the objective lens is fully illuminated by the incoming optical beam. The typical beam diameter of the He-Ne lasers used is approximately 2mm , less than the lens diameter of 5.72mm . To overcome this problem the beam is expanded before the lens using a beam expander.

The transmitted light from the waveguide was collected using a $\times 25$ microscope objective and focused on to the camera placed approximately 43cm from the output objective. The magnification M of the light collected by the camera was calculated using the equation

$$M = M_0 \left(1 + \frac{L}{fM_0}\right) \quad (14)$$

where f is the effective focal length of the objective, L is the increase in distance from the object compared to the working distance of the objective and M_0 is the magnification at the working distance of the objective. For the $\times 25$ lens the magnification is calculated to be approximately 80.

3.4 Back-reflection method

This method requires the end-fire coupling of laser light into a planar waveguide, as sketched in Fig. 3.4.1. The power exiting the waveguide (P_{out}) and the power back-reflected by the output face of the waveguide and transmitted at the input face (P_{back}) are measured by two photodetectors. Assuming P as the power impinging on the output face, we can get

$$P_{out} = P \cdot T_{w-a} \quad (15)$$

$$P_{back} = P \cdot (1 - T_{w-a}) \cdot e^{-\alpha L} \cdot T_{w-a} \quad (16)$$

where L is the length of the waveguide, while T_{w-a} and α are the waveguide-air transmittance and the attenuation coefficient. Here, T_{w-a} can be calculated by the well-known Fresnel transmission equations. By dividing Eq. (15) by Eq. (16), a straightforward expression relating the attenuation coefficient to the above powers is obtained:

$$a = \frac{1}{L} \log \frac{P_{out} \cdot (1 - T_{w-a})}{P_{back}} \quad (17)$$

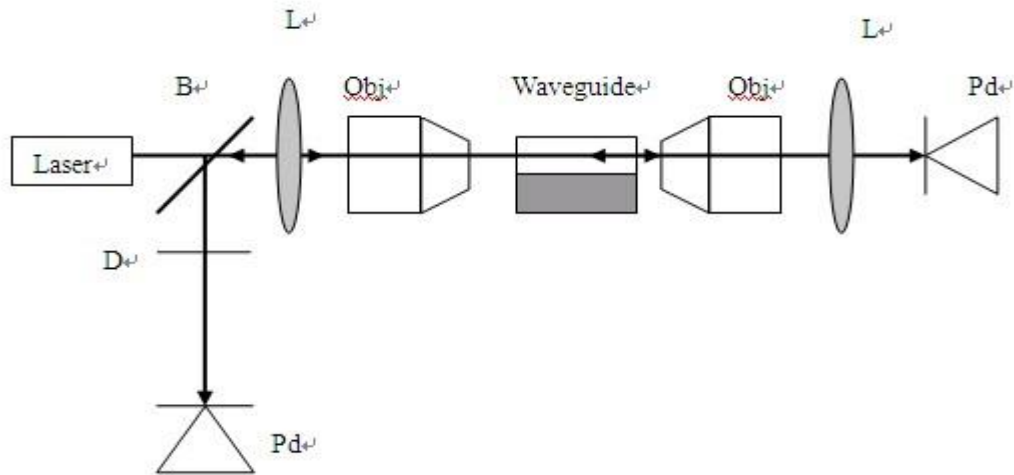


Fig. 3.4.1 Schematic setup of back-reflection (B: Beam splitter, L: lens, Obj: 25×Microscope objective, Pd: Photodetector, D: Diaphragm)

In order to obtain an accurate evaluation of the waveguide losses, some considerations must be taken into account [5]: (1) the focal length of the lenses

must be chosen in order to obtain a weakly divergent beam inside the waveguide, both in the forward and in the backward direction; (2) the waveguide must be slightly tilted to avoid interference between the beam reflected at the input face of the waveguide and the beam back-reflected at the output face; (3) the input and output faces of the waveguide must be accurately polished, so as to avoid additional scattering losses. Moreover, it is worth noting that this method is particularly suited for materials having high refractive index since the back-reflected beam intensity is proportional to the reflectivity at the waveguide-air interface.

3.5 Fourier transform infrared spectroscopy

Fourier transform infrared spectroscopy (FTIR) is a technique which can be used to obtain an infrared spectrum of absorption of a sample. Chemical functional groups are known to absorb radiation at specific frequencies. The intensity of the absorption is related to the concentration of the component. Intensity and frequency of sample absorption are depicted in a two-dimensional plot called a spectrum. Intensity is generally reported in terms of percent transmittance, the amount of light that passes through it.

In this work, Perkin-Elmer Spectrum One FTIR Spectrometer is used to measure the transmission spectra of the ion implanted chalcogenide glass. The Perkin-Elmer Spectrum One FTIR Spectrometer is capable of data collection over a wave number range of 370-7800 cm^{-1} . It can be configured to run in single-beam, ratio, or interferogram modes. The best resolution is 0.5 cm^{-1} . Instruments are interfaced to Perkin Elmer Spectrum software, which gives the user the ability to extract both qualitative and quantitative data from the spectrum, and generate custom reports.

3.6 Raman spectroscopy technique

3.6.1 Origins of Raman scattering

Raman spectroscopy is a spectroscopic technique based on inelastic scattering of monochromatic light from a laser source. Inelastic scattering means that the frequency of photons in monochromatic light changes upon interaction with a sample. Photons of the laser light are absorbed by the sample and then reemitted. Frequency of the reemitted photons is shifted up or down in comparison with original monochromatic frequency, which is called the Raman effect. This shift provides information about vibrational, rotational and other low frequency transitions in molecules. Raman spectroscopy can be used to study solid, liquid and gaseous samples.

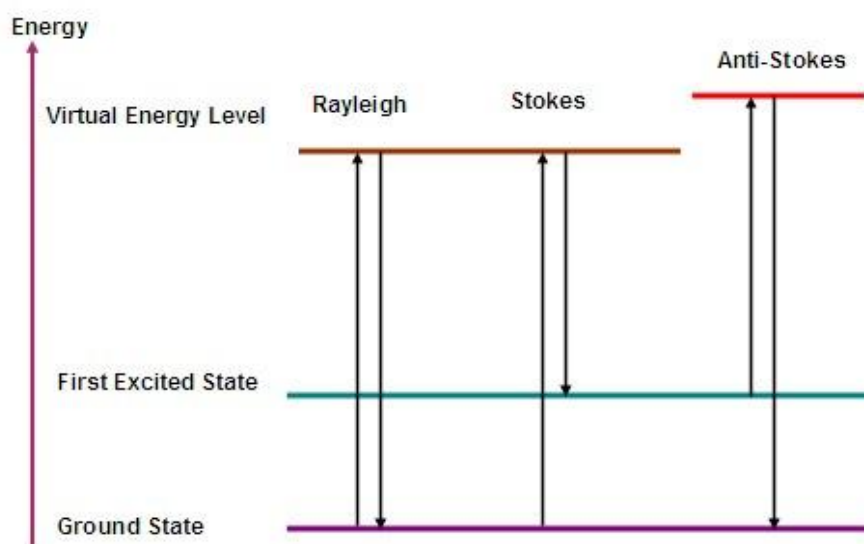


Fig. 3.6.1 Energy level diagram showing the states involved in Raman signal

The monochromatic laser light with frequency ν_0 excites molecules of the sample and transforms them into oscillating dipoles. Such oscillating dipoles emit light of three different frequencies (Fig.3.6.1):

1. A molecule with no Raman-active modes absorbs a photon with the

frequency ν_0 . The excited molecule returns back to the same basic vibrational state and emits light with the same frequency ν_0 as an excitation source. This type interaction is called an elastic Rayleigh scattering.

2. A photon with frequency ν_0 is absorbed by Raman-active molecule which at the time of interaction is in the basic vibrational state. Part of the photon's energy is transferred to the Raman-active mode with frequency ν_m and the resulting frequency of scattered light is reduced to $\nu_0 - \nu_m$. This type interaction is called Stokes Raman scattering.
3. A photon with frequency ν_0 is absorbed by a Raman-active molecule, which at the time of interaction is already in the excited vibrational state. Excessive energy of excited Raman active mode is released, molecule returns to the basic vibrational state and the resulting frequency of scattered light goes up to $\nu_0 + \nu_m$. This type interaction is called Anti-Stokes Raman scattering.

About 99.999% of all incident photons in spontaneous Raman undergo elastic Rayleigh scattering. This type of signal is useless for practical purposes of molecular characterization. Only about 0.001% of the incident light produces inelastic Raman signal with frequencies $\nu_0 \pm \nu_m$. Spontaneous Raman scattering is very weak and special measures should be taken to distinguish it from the predominant Rayleigh scattering. Instruments such as notch filters, tunable filters, laser stop apertures, double and triple spectrometric systems are used to reduce Rayleigh scattering and obtain high-quality Raman spectra.

3.6.2 Renishaw Ramascope instrumentation

Renishaw Ramascope system typically consists of four major components (Fig. 3.6.2):

1. Wavelength selector.
2. Sample illumination system and light collection optics.
3. Detector

4. Excitation source (Laser).

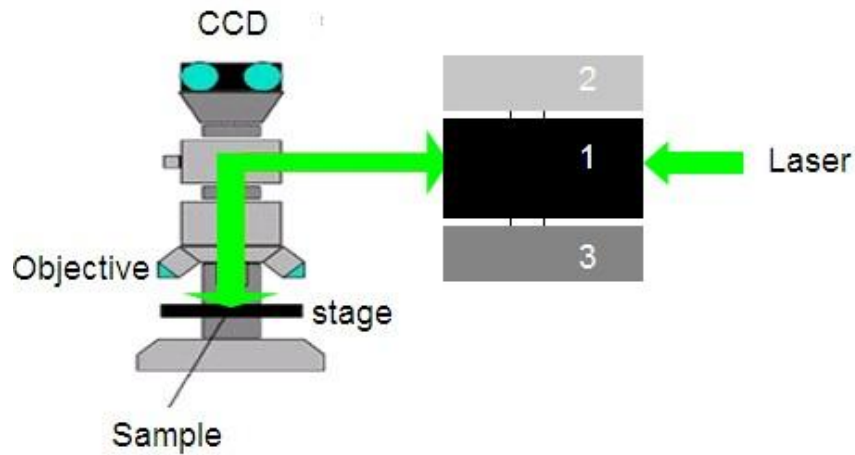


Fig. 3.6.2 Renishaw Ramascope system (1 Wavelength selector; 2 Sample illumination system and light collection optics; 3 Detector)

A sample is mounted on an XY motorized stage with a spatial resolution of $0.1\mu\text{m}$. The sample is illuminated by a laser beam with the wavelength of 514nm . The laser beam is focused on the sample through a microscope objective (with the smallest beam spot of $1 \pm 0.01\mu\text{m}$ in diameter). Through the CCD camera, it can be seen the position of laser spot on the sample. Scattered light is collected by the same objective and is sent through wavelength selector which cuts off the spectra of Rayleigh scattering. Then, the light is collected by light collection setup and Raman spectra of a sample can be obtained by a detector.

References

1. P.K. Tien, S. R. Sanseverino and R.J. Martin, *Phys. Lett.* 14, 503 (1974).
2. R. Ulrich and W. Prettl, *Appl. Phys.* 1, 55 (1973).
3. P. J. Chandler and F. L. Lama, *Opt. Acta* 33 127, (1986).
4. P. D. Townsend, P.J. Chandler, and L. Zhang, *Optical Effects of Ion Implantation*, Cambridge University Press, Cambridge, 1994.
5. R. Ramponi, R. Osellame and M. Marangoni, *Rev. Sci. Instrum.* **73**, 1117 (2002).

Chapter 4 Conventional ion implantation

This section presents the results obtained from the proton implanted gallium lanthanum sulphide (GLS) glass waveguide and the double proton implanted titanium doped gallium lanthanum oxysulfide (Ti:GLSO) glass waveguide. The proton implanted GLS waveguides provide some basic parameters to help in the design of ion implanted GLS waveguides in future. Ti:GLSO glass waveguide may be a candidate of tunable lasers and has a possibility to take place of versatile but expensive Ti-sapphire lasers.

4.1 Proton-implanted planar waveguide in GLS glass

4.1.1 Introduction

Chalcogenide glasses are novel materials with very promising properties [1]. As mentioned in chapter 2, GLS glass has significant advantages over other kinds of chalcogenide glasses from the view-point of application to optical devices: its wider transmission window, larger Kerr nonlinear coefficient, lower toxicity, excellent thermal and mechanical stabilities, and higher solubility for rare-earth dopants.

There are several techniques to fabricate waveguides in optical materials. To name a few, they are diffusion of metal ions, ion exchange, ion implantation, sputtering, chemical vapor deposition, and laser beam writing. Thin GLS film waveguides have been fabricated by spin coating and pulsed laser deposition [2]. However, at least three stages are needed for spin coating method, which means the fabrication process is complicated, and sulfur deficiency exists in the GLS film for the pulsed laser deposition method. Femtosecond laser writing can also be used for GLS glass waveguide fabrication [3], but only buried

channel waveguides can be fabricated in most cases.

With respect to ion implantation technique, He^+ implantation has also been used to form waveguides in As_2S_3 glass thin films. However, only light confinement was observed and no data on the propagation loss and the profile of refractive index are available [4]. In this part, the planar waveguide in GLS glass is fabricated by proton implantation, and the relevant properties of the waveguide are characterized.

4.1.2 Experimental

The GLS glass plate of $15 \times 15 \times 5 \text{ mm}^3$ was optically polished. One facet ($15 \times 15 \text{ mm}^2$) of GLS glass was implanted by protons at the energy of 350 keV and the dose of $1 \times 10^{15} \text{ atoms/cm}^2$ at room temperature, using the ion implantation equipment at Ion Technology Center Co., Ltd, Japan.

The prism coupling method was used to observe the guided TE mode spectrum of the waveguide using a Model 2010 Prism Coupler. The top and bottom faces (two $15 \times 15 \text{ mm}^2$ faces) of the implanted and un-implanted samples were cleaned carefully, and transmission spectra ($7800\text{-}1000 \text{ cm}^{-1}$) were measured at room temperature using Fourier transform infrared (FTIR) spectrometer (Perkin Elmer Spectrum One). The optical loss was measured by the back-reflection method.

4.1.3 Experimental Results and Discussion

Figure 4.1.1 shows the relative intensity of TE polarized light reflected from the prism versus the effective refractive index of the planar waveguide. One can see clearly that two TE modes (effective indices are 2.4454 and 2.4423) have been excited in this waveguide as a result of the implantation. Both effective refractive indices are lower than the substrate refractive index; therefore there must be a typical optical barrier formation to confine the light between the

waveguide surface and the substrate [5].

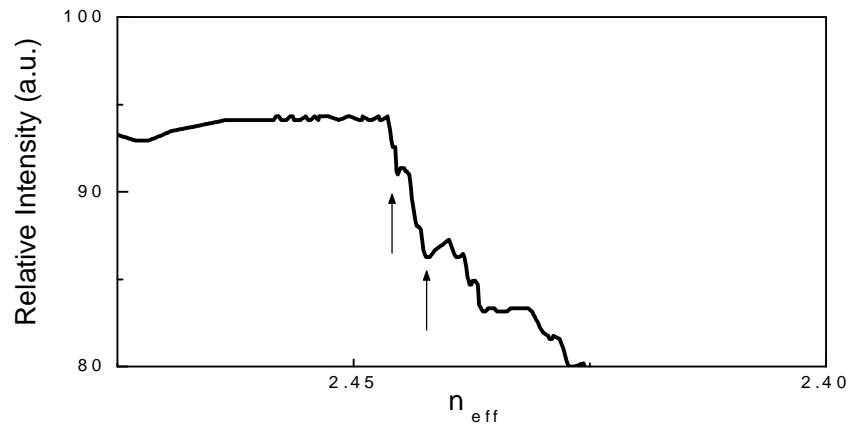


Fig. 4.1.1 TE mode spectrum of the planar waveguide

Because there are only two modes in the waveguide, we can not use traditional RCM directly to simulate its refractive index profile. Considering the two modes and RCM, here we can suppose a refractive index profile and use the beam propagation method (BPM) to simulate the intensity distribution according to the supposed profile. By adjusting the parameters of the supposed profile, the refractive index distribution can be obtained when the simulated intensity distribution Fig. 4.1.2(a) is in a reasonable agreement with the measured one Fig. 4.1.2(b). The obtained result is shown in Fig. 4.1.3, and the refractive index of the substrate is indicated by a dotted line. We see that the surface refractive index (RI) of the implanted sample is only slightly larger than the substrate, and RI decreases by about 0.5% at the barrier which is located about $2.9\mu\text{m}$ beneath the surface. In this case, only the low index barrier is functioning to confine the light.

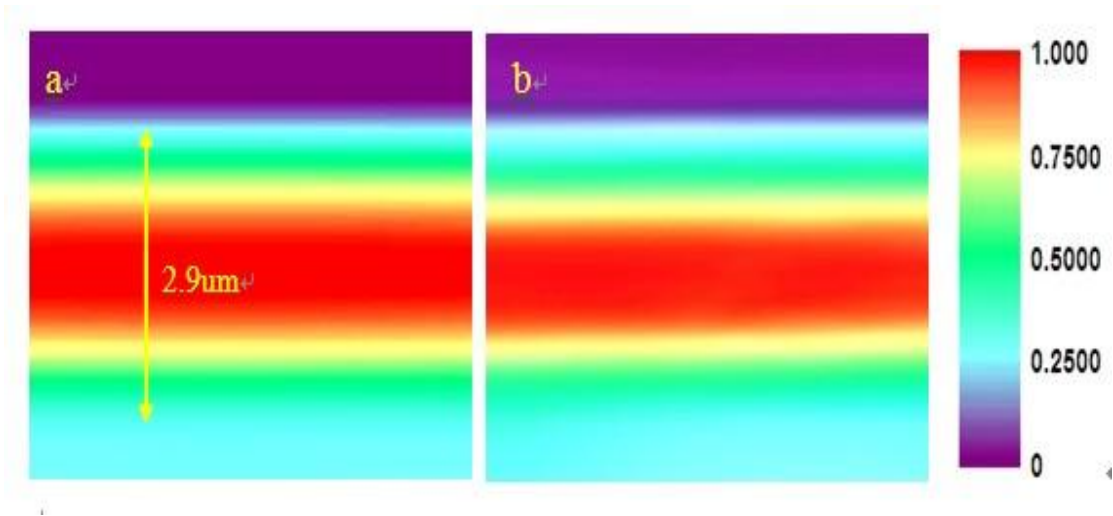


Fig. 4.1.2 Near-field pattern at the output plane of the planar waveguide (a) simulated by BPM (b) measured result

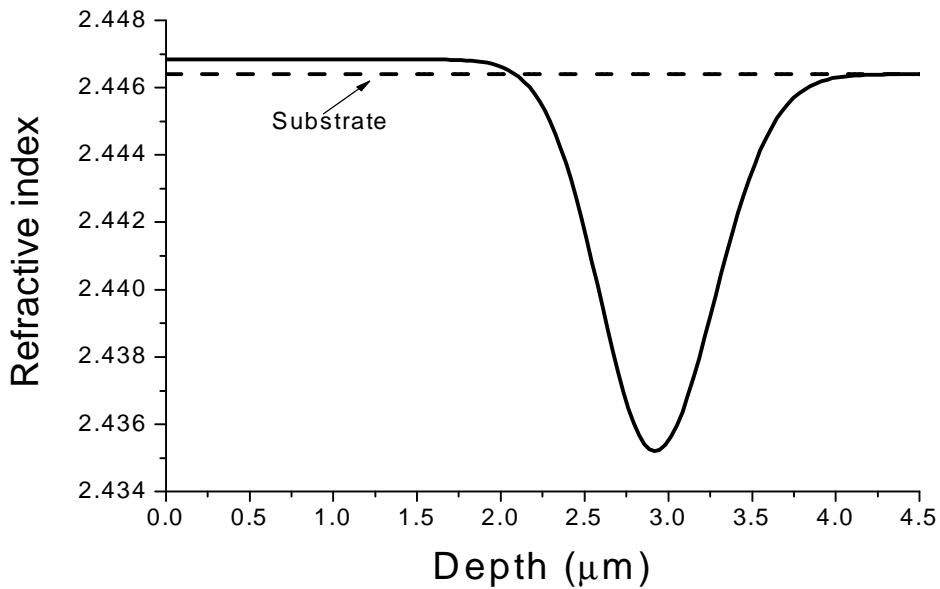


Fig. 4.1.3 Refractive index profile of the waveguide

The mechanism of the waveguide formation in glass is usually complicated because of the complex composition and disordered structures of glass. In the case of light ion (H or He) implanted glass waveguides, the violent collisions between the incident ions and target nuclei mainly occur at the end of the ion range. The nuclear damage caused by these collisions is the main reason for the

reduction of the refractive index of glass to generate an “optical barrier” [6-8]. On the other hand, within the region between this barrier and the surface, the nuclear damage is quite small and the electronic effect is dominant. However, the ionization processes caused by electronic energy deposition have only slight effect on the change of refractive index [5, 9]. Thus, the region between air and the optical barrier is sandwiched by low-refractive index regions, which acts as waveguides. To estimate the energy loss, SRIM’ 2008 (<http://www.srim.org>) was used, and the obtained results are shown in Fig. 4.1.4. From the discussions above, we can conclude that the electronic excitation mainly contributes to the increase in refractive index and nuclear collisions generate the barrier in the present energy range of proton implantation in GLS glass, although the detailed physics behind this is not clear yet.

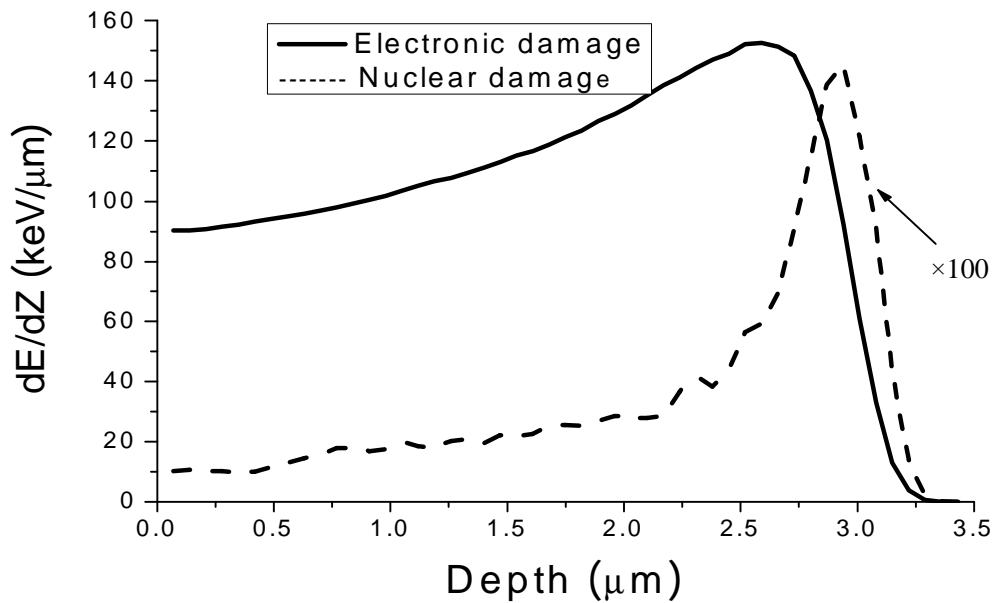


Fig.

4.1.4 Energy loss based on SRIM 2008

Implantation-induced color centers can sometimes cause the additional absorption in the implanted samples [6, 7]. Therefore, it is necessary to check the transmission spectra of implanted samples. Figure 4.1.5 shows the vertical

transmission spectra of the un-implanted and implanted samples in the wavelength range of 1.28 -10 μm in which GLS glass is mainly used. Both spectra almost overlap perfectly and indicate that proton implantation does not affect the transmission property in the range of 7800-1500 cm^{-1} (1.28-6.67 μm). The transmittance is even improved in the range of 1500-1000 cm^{-1} (6.67-10 μm), though the reason is as yet not well understood.

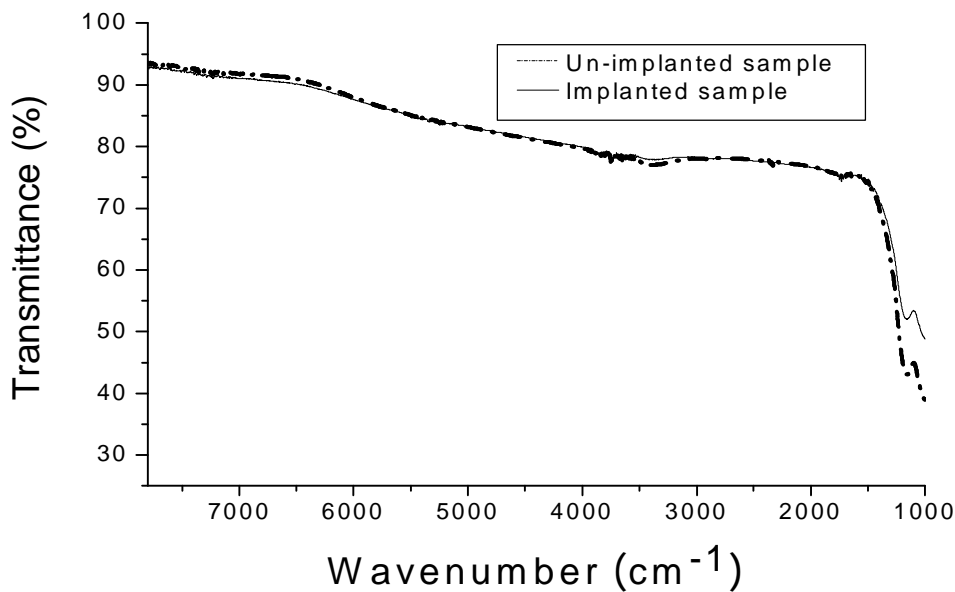


Fig. 4.1.5 Comparison of transmission spectra for the un-implanted and implanted samples

One of the most important features of a waveguide is its optical loss. Many methods have been used to evaluate loss of planar waveguides, including collection of scattered light [8], the Fabry-Perot technique [9], the isosceles-prism method [5] and the back-reflection method [5]. As mentioned in last chapter, among these methods, the back-reflection method can be successfully applied to short waveguides and is particularly suited for waveguides realized on high refractive index substrates. The propagation loss of the waveguide in the present work results in approximately 3.2 dB/cm at the wavelength of 632.8 nm.

The quality of end-face polish is highly important for the back-reflection method. The scattering loss at the output face due to a poor polishing quality leads to a lower estimate of P_{out} and thus to an increased value of the attenuation. Our preliminary observation of the near field pattern suggests that the polished end-face is not perfectly smooth. Therefore, the real propagation loss may be less than 3.2 dB/cm.

The implantation process generates color centers (optical absorption sites) owing to electronic energy deposition and destroys to some extent the equilibrium of the original structure by nuclear collisions. Both of these effects inevitably increase the waveguide loss; therefore, annealing treatment is commonly used for all the ion-implanted waveguides. The planar waveguide in our work was examined without annealing. The propagation loss must be improved after annealing at an appropriate temperature.

From Fig. 4.1.2, we can see clearly that some light leaks through the barrier into the substrate due to optical tunneling effect [10] which is common to all barrier-confined waveguides. This tunneling is another reason for the propagation loss. It is suggested that multi-energy implantation to broaden the barrier or a larger dose to induce a larger refractive index reduction at the barrier is needed to reduce the tunneling loss in the future.

4.1.4 Conclusions

We demonstrate that the planar waveguide can be realized on the GLS glass substrate using 350keV, 1×10^{15} atoms/cm² protons implantation. We have found two modes existing in the waveguide, and obtained the refractive index profile by comparing the simulated intensity distribution with the measured one. The implanted sample shows good transmission at the wavelength range of 1.28-10 μm . The optical loss of the present waveguide is estimated to be about 3.2 dB/cm, which is a reasonable value and can be improved by annealing. All

these results may help in the design of proton implanted GLS waveguides. We believe that improved proton implanted GLS glass waveguides have a great potential and play a crucial role in developments of integrated optical devices.

4.2 Ion implanted Ti:GLSO glass waveguide as a candidate of tunable lasers

4.2.1 Introduction

Chalcogenide glasses possess a number of desirable properties that make them attractive for fabricating planar optical waveguides. Based on their high linear refractive index and broad infrared transparency, chalcogenide glass waveguides integrated with quantum cascade lasers have been realized for on-chip mid-IR photonic circuits [11]. Their large ultra-fast third order optical nonlinearity has been successfully used for processing of telecommunications signals [12]. Finally, their low phonon energy makes them as attractive hosts for metal elements doping, which could lead to waveguide lasers operating at the wavelengths that are weakly or not observed in oxide-based glasses.

Though chalcogenide glass fibers doped with rare earth elements have been studied for active applications [1, 13], we note that reports in the literature of active waveguides are scarce. It appears that the common chalcogenide glasses suffer from poor rare-earth solubility (e.g. As_2S_3) [1] or low glass transition temperature (e.g. As_2Se_3) [14], both of which cause this scarcity. So far, gallium lanthanum sulfide (GLS) glass [15-17] seems to be the only one glass well-suited for active waveguides. Its high glass transition temperature ($T_g=580^\circ\text{C}$) makes GLS appropriate for applications in high temperature. High rare earth dopant concentrations without clustering are possible owing to the fact that the rare earth ions substitute for the lanthanum ions in the glass matrix [16]. The waveguide laser and amplifier have been realized in Nd and Er doped

GLS glass, respectively [18, 19]. Compared with Nd or Er, the transition metal titanium doped GLS (Ti:GLS) and gallium lanthanum oxysulfide (Ti:GLSO) glasses are more attractive, because they may become new non-crystalline tunable solid state laser sources (800-1700nm) [20]. On the other hand, emissions from Ti have not been observed in common silicate and phosphate glasses.

Previous efforts to fabricate waveguides in GLS have utilized UV-laser writing or thin film sputtering [18, 19]. However, the absorption band of Ti in GLS or GLSO glass can not be fully resolved [20], which could cause problems when the laser wavelength overlaps with the Ti absorption band. Thin film sputtering may induce the composition of the film different from that of the bulk [19]. In this section, we describe the fabrication process for the Ti:GLSO waveguide using proton implantation, measure the relevant optical properties, and explain the mechanisms of waveguide formation.

4.2.2 Waveguide fabrication

Firstly, 350keV proton with the dose of 1×10^{15} ions/cm² was implanted to fabricate waveguide in gallium lanthanum oxysulfide (GLSO) glass (molar ratio 75Ga₂S₃:25La₂O₃). According to the reconstructed refractive index profile, the waveguide exhibits a “barrier confinement” type index profile (not shown here for brevity), which means that the low refractive index layer generated by nuclear damage is buried inside the substrate and the guiding layer (due to electronic damage) with small index change (+0.0002) is formed between the surface and barrier. The propagation loss of the GLSO waveguide is ~ 17dB/cm. Based on the simulation using beam propagation method, most of the loss

(~14.7dB/cm) is caused by the tunneling effect [10], which is attributed to the optical barrier not thick enough. On the other hand, the loss caused by other factors due to implantation (e.g. absorption, scattering) is low, which gives our confidence to apply double proton implantation to generate optical waveguides in Ti:GLSO glass.

The Ti:GLSO glass consists of $75\text{Ga}_2\text{S}_3:24.5\text{La}_2\text{O}_3:0.5\text{Ti}_2\text{S}_3$. The refractive index of the glass is 2.2798. The sample was first implanted by 470keV proton with the dose of 1×10^{16} ions/cm² and then 500keV proton with the dose of 2×10^{16} ions/cm². From the nuclear energy deposition results (Fig. 4.2.1) calculated by SRIM 2010 code, the optical barrier is at least 1 μm thicker than that of 350keV implantation case (such barrier is created by the nuclear damage of implanted ions). Considering the higher dose of double proton implantation, it is reasonable to estimate that the refractive index decrease in the barrier region is larger than that of the 350keV implanted waveguide. Thus, we can simulate the light intensity approximately by assuming a refractive index distribution (refer the index of 350keV implanted waveguide). It is found all light confined in the guiding layer.

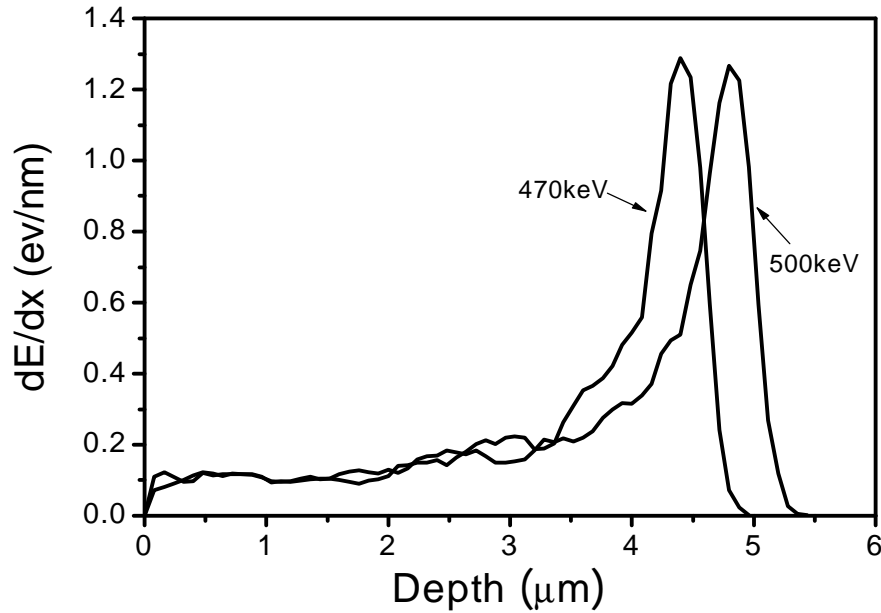


Fig. 4.2.1 Nuclear energy loss of the proton ion implantation

After polishing the end faces, the near-field pattern was measured by an end-fire coupling system at the wavelength of 632.8nm. The propagation loss (632.8nm) was measured by back-reflection method. A Renishaw Ramascope setup was used for Raman back-scattering measurement. The sample was mounted on an XY motorized stage with a spatial resolution of 0.1 μ m. The laser beam (514nm) was focussed onto the cross-section with a spot of $1 \pm 0.01\mu$ m in diameter. The measurements were carried out from the implanted surface to the substrate with an increment of 1 μ m.

4.2.3 Guiding property results

The refractive index distribution is usually measured by prism coupling method. However, since the present sample thickness is rather thin (0.5mm), we choose the following method. Firstly, it is reasonable to assume that the index change at the guiding layer is quite small (compared with the substrate), because the electronic damage of double proton implantation (not shown) is in the same order of that of 350keV proton implantation. Moreover, the barrier

position can be estimated according to Fig. 4.2.1, as already mentioned in last part. With these index mappings, the refractive index distribution can be obtained by simulating the waveguide mode for different index profiles until a good agreement between the calculated mode and experimental one (Fig. 4.2.2(a)). Figure 4.2.2 (b) shows the simulated mode when the refractive index profile is assumed as Fig. 4.2.3(a). The refractive index increases slightly (+0.0001) in the guiding region. The barrier with negative index change is about 3um thick (from 2.7-5.7 um), which is caused by the nuclear damage of double proton implantation. As shown in Fig. 4.2.2 (a), all the light is confined in the guiding region due to the barrier thick enough, which is consistent with our prediction. Note that the waveguide does not exhibit birefringence through observing near-field patterns.

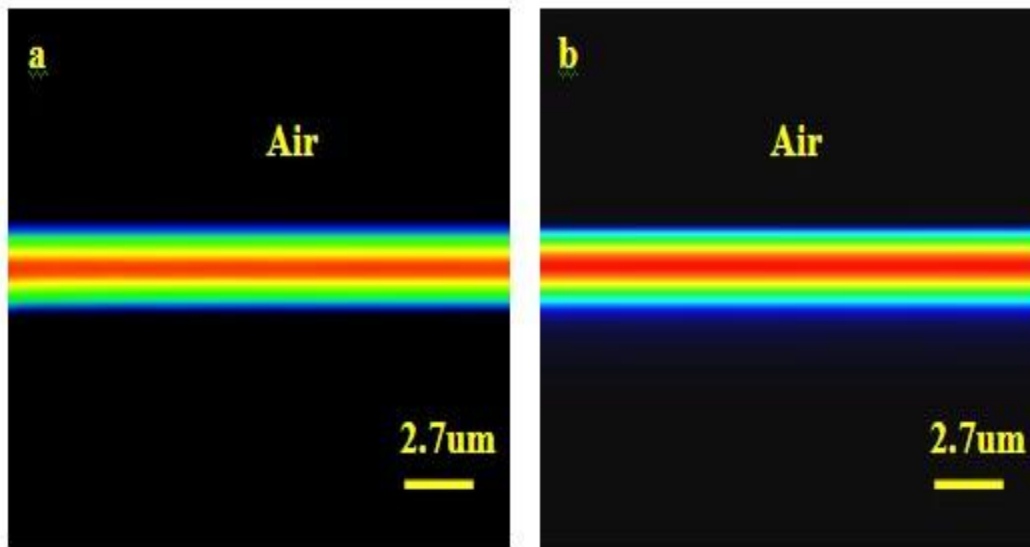


Fig. 4.2.2 The measured (a) and simulated (b) near field patterns

The propagation loss of the implanted waveguide is ~ 7.5 dB/cm. Given the material absorption of ~ 7.0 dB/cm due to Ti doping [20] and surface scattering, the ion implantation induces little point defects (color centers) in the guiding region, which means that the waveguide structure is almost as perfect as the original glass.

4.2.4 Raman spectra analysis

The mechanisms of ion implanted glass waveguide formation are usually complicated. So far, only α -SiO₂ waveguides have been characterized clearly. In that case, only guiding layer with an increased refractive index is generated (without a barrier), and this index enhancement originates from the compaction of silica. Raman spectroscopy has been proven to be a valuable tool to reveal the structure changes that occur in ion implanted crystal substrates [21, 22]. In this work, it is first time applied to analyze glass samples.

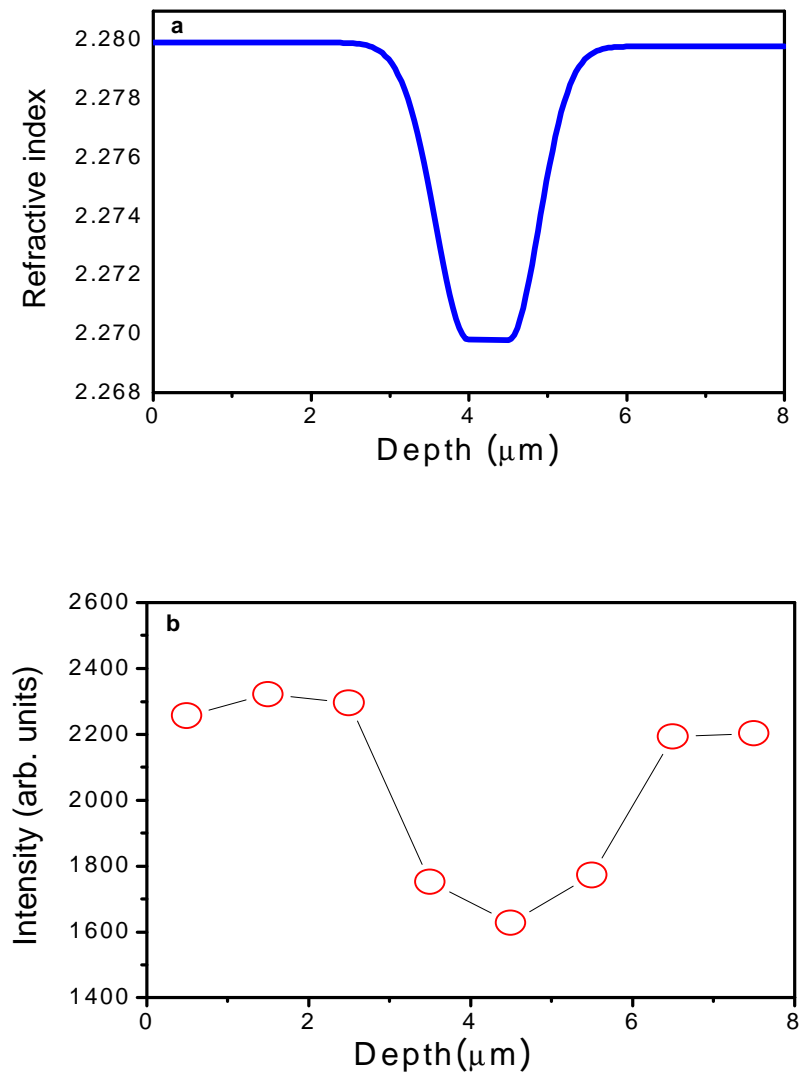


Fig. 4.2.3(a) The reconstructed refractive index profile. (b) Depth profile of the Raman intensity of the 328 cm⁻¹ peak

Figure 4.2.4 illustrates the Raman spectra of three regions, i.e. guiding (curve 1), barrier (curve 3) and substrate (curve 2). The Raman mode at $\sim 328\text{cm}^{-1}$ can be attributed to the symmetrical stretching vibrations of GaS_4 tetrahedra [23]. The main Raman feature is that the intensity in the barrier is noticeably smaller than that of the other two regions. This intensity decrease should be caused by the glass matrix expansion induced by the collisions between the incident proton ions and substrate atoms. According to the Lorentz-Lorenz equation, the refractive index change Δn is described as,

$$\frac{\Delta n}{n} = \frac{(n^2 - 1)(n^2 + 2)}{6n^2} \left(-\frac{\Delta V}{V} + \frac{\Delta \alpha}{\alpha} + F \right)$$

where ΔV is the volume change, $\Delta \alpha$ the bond polarizability, and F is the structure factor. As a result, it is reasonable that the volume expansion ($\Delta V > 0$) mainly results in the barrier formation in the proton implanted Ti:GLSO waveguide.

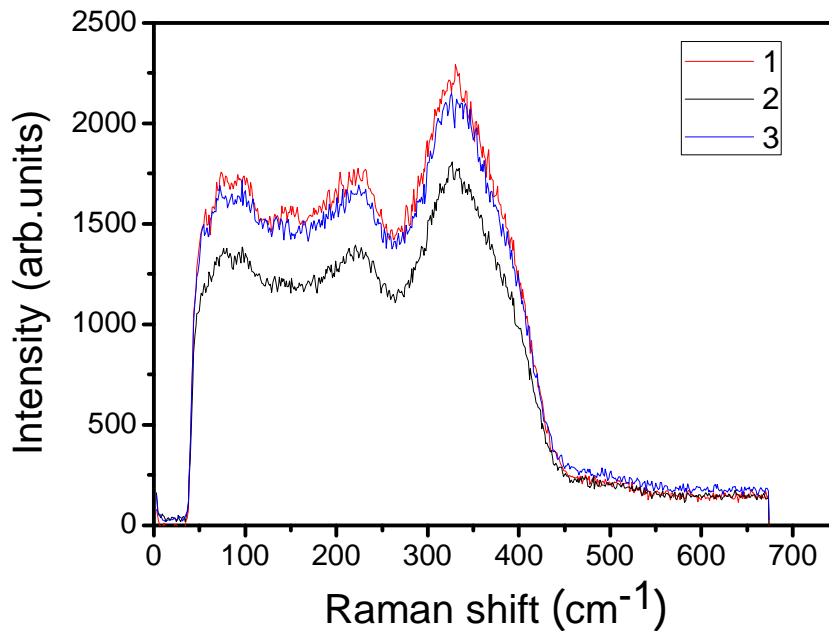


Fig. 4.2.4 The Raman spectra of guiding layer (1), substrate (2) and barrier (3)

Figure 4.2.3 (b) shows that the intensity of the 328 cm^{-1} peak varies with depth. Comparison with Fig. 4.2.3(a) exhibits good correlation between the change of Raman intensity and the variation of the refractive index of the glass. In Fig. 4.2.3 (b), the Raman intensity between the guiding region and substrate is only slightly different due to the uncertainty in the experiment. This means that the electronic damage induces little change in the glass matrix, which agrees with the conclusion from the propagation loss measurement.

4.2.5 Conclusion

Based on the 350keV proton implantation experiment and approximate design, a planar waveguide is fabricated by double proton implantation. The refractive index distribution is reconstructed according to the near-field pattern. Through Raman characterizations, it is found that the glass matrix expansion due to nuclear damage causes the barrier formation. We have found low optical loss caused by ion implantation and little structure change in the guiding layer. These are necessary conditions for future realization of waveguide lasers in Ti::GLSO glass.

References

1. A. Zakery and S.R. Elliott, *J. Non-Crystal. Solids* 330, 1 (2003).
2. M. Hughes, W. Yang, and D. Hewak, *Appl. Phys. Lett.* 90, 131113 (2007).
3. Y. J. Weng, Y. C. Weng, H. S. Fang, and S. Y. Yang, *Jpn. J. Appl. Phys.* 48, 116502 (2009).
4. J. Viens, C. Meneghini, A. Villeneuve, T. Galstian, E. Knystautas, M. Duguay, K. Richardson, and T. Cardinal, *J. Lightwave Technol.* 17, 1184 (1999).
5. P.D. Townsend, *Rep. Prog. Phys.* 50, 501 (1987).
6. F. Chen, X. L. Wang, X. S. Li, L. L. Hu, Q. M. Lu, K. M. Wang, B. R. Shi, and D. Y. Shen, *Appl. Surf. Sci.* 193, 92 (2002).
7. Z. Zhuo, E. Y. B. Pun, and S. F. Wong, *J. Mater. Res.* 16, 1135 (2001).
8. P. J. Chandler, L. Zhang, and P. D. Townsend, *Solid State Phenom.* 27, 129 (1992).
9. F. Chen, *J. Appl. Phys.* 106(8), 081101 (2009).
10. P. D. Townsend, P.J. Chandler, and L. Zhang, *Optical Effects of Ion Implantation*, Cambridge University Press, Cambridge, 1994.
11. C. Tsay, F. Toor, C.F. Gmachl, and C. B. Arnold, *Opt. Lett.* 35 (20), 3324 (2010).
12. M. D. Pelusi, V. G. Ta'eed, L. B. Fu, E. Magi, M. R. E. Lamont, S. Madden, D. Y. Choi, D. A. P. Bulla, B. Luther-Davies, and B. J. Eggleton, *IEEE J. Sel. Top. Quantum Electron.* 14(3), 529 (2008).
13. A. Mori, Y. Ohishi, T. Kanamori, and S. Sudo, *Appl. Phys. Lett.* 70, 1230(1997).
14. R. G. Decorby, N. Ponnampalam, M. H. Pai, H. T. Nguyen, P. K. Dwivedi, T. J. Clement, C. J. Haugen, J. N. McMullin, and S. O. Kasap, *IEEE J. Sel. Top. Quantum Electron.* 11, 539 (2005).

15. T. Schweizer, D. W. Hewak, D. N. Payne, T. Jensen, and G. Huber, *Electron. Lett.* 32, 666(1996).
16. D. W. Hewak, R. C. Moore, T. Schweizer, J. Wang, B. Samson, W. S. Brocklesby, D. N. Payne, and E. J. Tarbox, *Electronics Lett.* 32, 384(1996).
17. A. K. Mairaj, R. J. Curry, and D. W. Hewak, *Electronics Lett.* 40, 421 (2004).
18. A. K. Mairaj, C. Riziotis, A. M. Chardon, P. G. R. Smith, D. P. Shepherd, and D. W. Hewak, *Appl. Phys. Lett.* 81, 3708 (2002).
19. J. A. Frantz, L. B. Shaw, J. S. Sanghera, and I. D. Aggarwal, *Opt. Express* 14, 1797 (2006).
20. M. A. Hughes, R. J. Curry, and D. W. Hewak, *J. Opt. Soc. Am. B* 25 (9), 1458 (2008).
21. A. Ródenas, G. A. Torchia, G. Lifante, E. Cantelar, J. Lamela, F. Jaque, L. Roso, and D. Jaque, *Appl. Phys. B: Lasers Opt.* 95, 85 (2009).
22. S. M. Kostritskii and P. Moretti, *J. Appl. Phys.* 101, 094109 (2007).
23. T. Schweizer, F. Goutaland, E. Martins, D. W. Hewak, and W. S. Brocklesby, *J. Opt. Soc. Am. B* 18, 1436-1442(2001).

Chapter 5 Swift-heavy ion implantation

In this chapter, swift-heavy ion implantation (SHI) is used to fabricate planar waveguides in GLS and GLSO glass, Nd:YAG crystal and rare-earth doped GLS glass. Firstly, we fabricate optical GLS and GLSO glass waveguides using Ar^{4+} ion implantation at 60 MeV and 2×10^{12} ions/cm² and characterize relevant optical properties of the waveguides. Then, a buried planar Nd:YAG waveguide has been fabricated by 20MeV N ion implantation. From the Raman and optical characterization, the mechanisms of swift-heavy ion implanted Nd:YAG waveguide formation are analyzed. At last, planar waveguides are fabricated in Nd or Ho doped GLS laser glasses by 60MeV Ar or 20MeV N ion implantation and the different implantation effects are demonstrated.

5.1 Application of swift-heavy ion implantation to the formation of chalcogenide glass waveguides

5.1.1 Introduction

Conventional ion implantation, utilizing energies from several hundreds of keV to several MeV and fluences as high as 10^{15} - 10^{17} ions/cm², has been used to produce waveguides in many kinds of materials, including crystals, glasses and polymers, but such high fluences make it time-consuming [1]. Recently, the use of swift ion (with energies higher than 0.1 MeV/amu) implantation to fabricate optical waveguides has emerged. Its ultralow dose is the most distinguishing feature in contrast to conventional ion implantation. Swift and heavy ions with dose of 10^{12} - 10^{14} ions/cm² have been used to generate optical waveguides in crystals such as KGW, LiNbO₃ and Nd:YAG [2-10]. In these cases, the electronic energy loss is responsible for the refractive index change.

For KGW and LiNbO₃, a buried layer with lower refractive index is generated in the substrate, constituting an optical barrier to confine light propagation between this barrier and the surface. For Nd:YAG, a buried layer with higher refractive index is built, acting as the core of the waveguide. So far, nearly all studies have focused on crystal waveguides and only one reference [11] has concerned amorphous material waveguides. In this reference, J. Manzano et al used 5MeV F or 20MeV Cl ions to produce α – SiO₂ waveguides which showed a step-like refractive index distribution.

The purpose of present work is to study the application of swift and heavy ion implantation to the formation of chalcogenide glass optical waveguides. Chalcogenide glasses are novel materials with very promising properties [12]. According to our previous work in chapter 4, the electronic energy deposition can cause positive refractive index change (even very small) in the near-surface region of GLS and GLSO glass. Therefore, we expect that the large electronic energy loss of swift ion implantation can result in an enhanced index well and consequently the propagation loss can be decreased. In this part, we fabricate optical GLS and GLSO glass waveguides using Ar⁴⁺ at 60 MeV and 2×10^{12} ions/cm² and characterize relevant optical properties of the waveguides.

5.1.2 Experimental

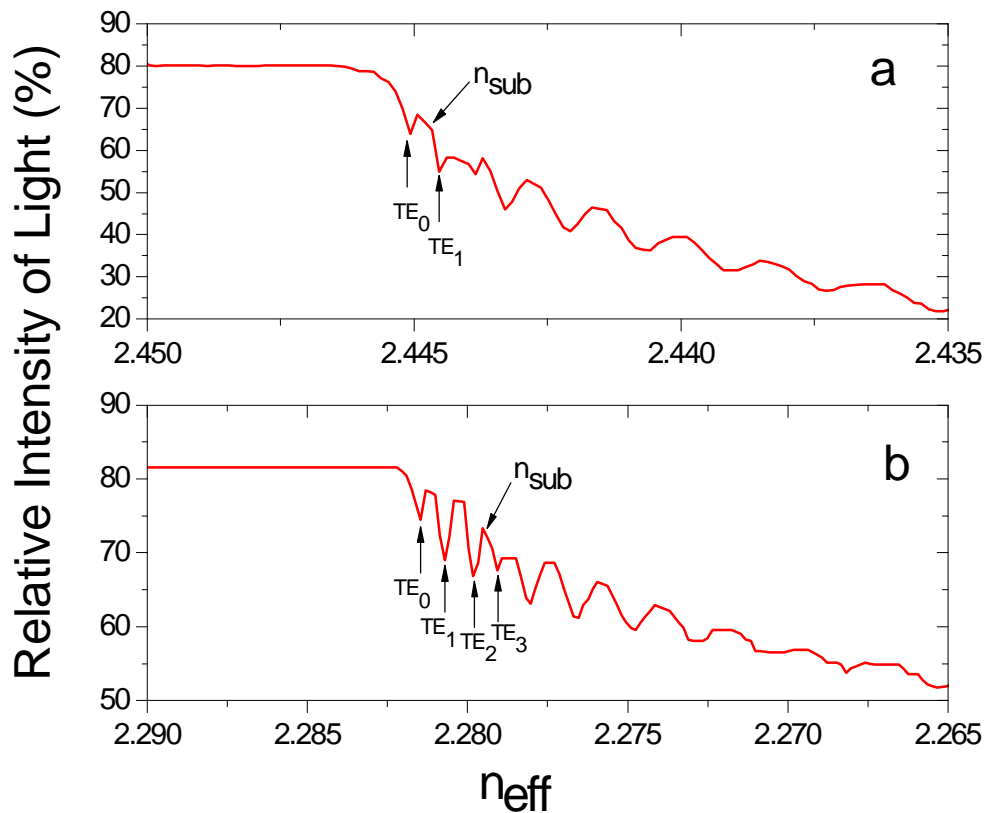
GLS and GLSO glasses of $10 \times 10 \times 2$ mm³ were irradiated with Ar⁴⁺ at 60 MeV and 2×10^{12} ions/cm², using tandem accelerator at Tokai Research and Development Center, Japan Atomic Energy Agency. The ion beam was focused on the sample surface and then scanned over the area of 10×10 mm² to achieve the dose uniformity. The beam current density was maintained at about 10 nA/cm² to minimize charging and heating effects during irradiation.

The implanted surfaces of GLS and GLSO glass were still smooth enough characterized by atomic force microscope. Then, prism-coupling technique was

used for the observation of the guided TE mode spectra of the waveguides at the wavelength of 632.8 nm and 1539 nm. After polishing the end-faces of the implanted glass, the near-field pattern of the transmitted light through the waveguides were measured by end-fire coupling. The optical loss was measured by the back-reflection method [14].

5.1.3 Results and Discussion

Figure 5.1.1 indicates the relative intensity of the reflected light versus the effective refractive index (n_{eff}) measured by prism-coupling method. The refractive indices of the substrate (n_{sub}) are 2.4447 (632.8 nm) and 2.3500 (1539 nm) for GLS glass and 2.2794(623.8 nm) and 2.2031(1539 nm) for GLSO glass (shown in Fig. 5.1.1).



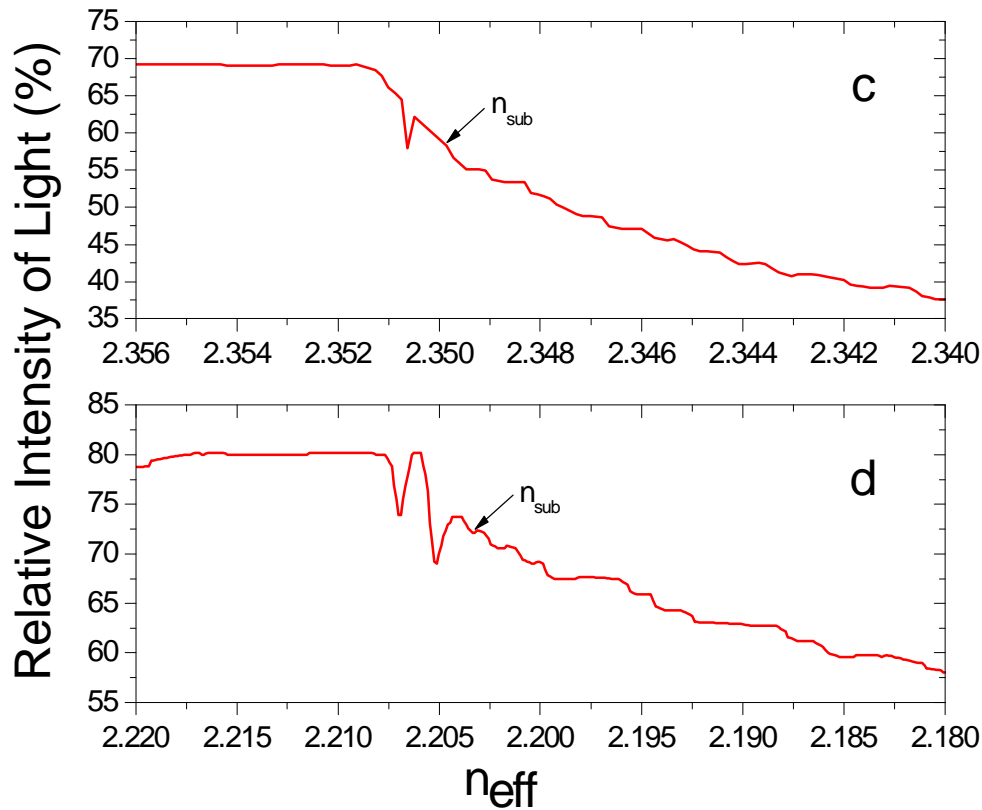


Fig. 5.1.1 TE mode spectra of the implanted waveguides at 632.8nm (a) GLS and (b) GLSO, and at 1539nm (c) GLS and (d) GLSO

As we can see, for GLS glass, the n_{eff} of TE_0 mode is higher than the n_{sub} at both wavelengths; for GLSO glass, the n_{eff} s of $\text{TE}_0 \sim \text{TE}_2$ modes at 632.8 nm and the two modes at 1539 nm are higher than the n_{sub} . These modes mean that near-surface regions of the glasses have a positive change after the implantation and the light inside the waveguides can propagate in a non-leaky manner [1]. The dip of TE_1 mode of the GLS waveguide or TE_3 mode of the GLSO waveguide is also sharp at 632.8nm. Moreover, we observed the near-field patterns of these two modes (not shown here). As a result, it can be concluded that an optical barrier exists in each of these waveguides to confine the light propagation. The other dips of GLS waveguide or the GLSO waveguide are clearly broader than the formers. This is probably the result of multiple optical

reflections occurring at the interfaces between the waveguide and the substrate [18]. The refractive index profiles are reconstructed by RCM [15] as shown in Fig. 5.1.2. It is found that the measured n_{eff} is in agreement with the calculated values (based on the reconstructed profiles of Fig. 5.1.2) within 10^{-4} .

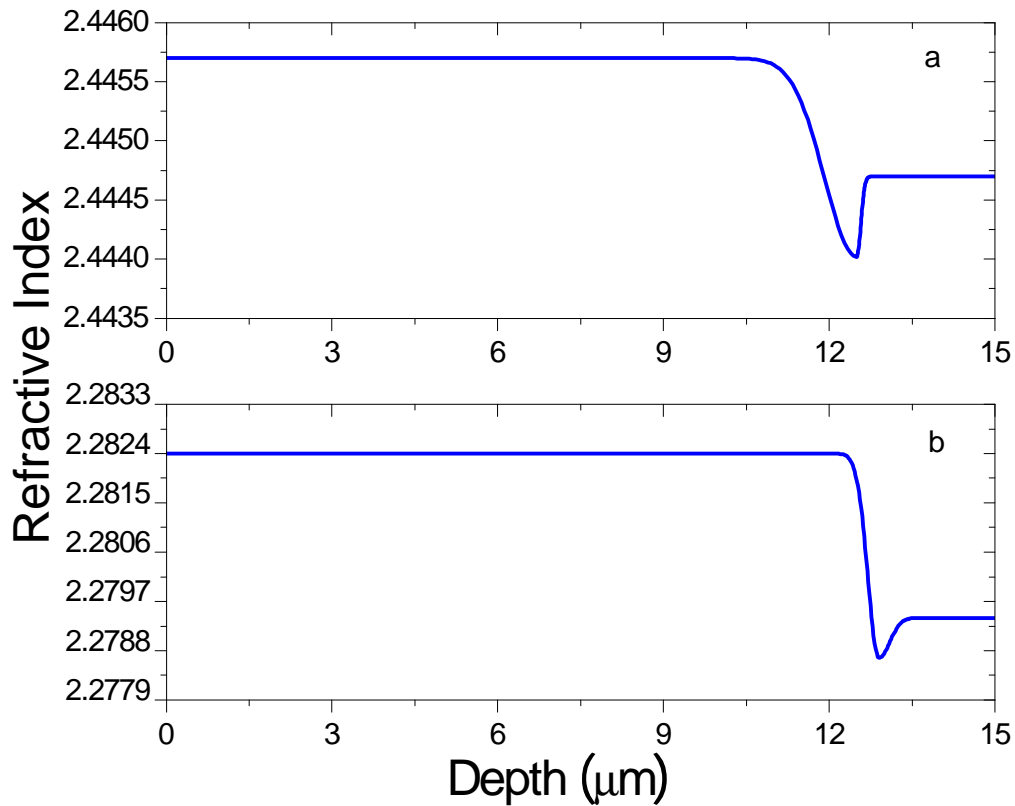


Fig. 5.1.2 Refractive index distributions of (a) GLS waveguide and (b) GLSO waveguide at the wavelength of 632.8nm

For further confirmation of the refractive index distributions, we performed a modal simulation according to Fig. 5.1.2 by using beam propagation method. Figure 5.1.3 (a) and (c) depict the calculated modal profiles of the TE_0 modes of the GLS and GLSO waveguides. Experimentally measured near-field intensity distributions of the TE_0 modes from the output facets are shown in (b) and (d).



Fig. 5.1.3 Near-field intensity distribution experimental result (a)GLS and (c)GLSO; simulation using BPM (b)GLS and (d)GLSO

By comparing Fig. 5.1.3 (a) and (b), and (c) and (d), respectively, we can conclude that the simulations agree well with the experimental data. Both index profiles exhibit the same “well + barrier” distributions: an enhanced index well with refractive index increase $\Delta n_i=0.1\%$ and a thickness $d\approx 10.6\ \mu\text{m}$ for GLS ($\Delta n_i=0.3\%$ and $d\approx 12.1\ \mu\text{m}$ for GLSO) is built in the near-surface region; a barrier with maximum refractive index decrease $\Delta n_d=0.07\%$ and a thickness $d'\approx 2.4\ \mu\text{m}$ for GLS ($\Delta n_d=0.08\%$ and $d'\approx 1.1\ \mu\text{m}$ for GLSO) is created at the end of the incident ion’s track. Moreover, we can see in Fig. 5.1.3 that the light is highly restricted within the waveguide region. The well confined light

propagation strongly suggests a possibility of channel waveguide fabrication by simply applying standard photolithographic procedures. The n_{eff} s were found unchanged after storage in air for two months, confirming the permanence of the induced refractive index change.

Figure 5.1.4 shows the relevant electronic and nuclear energy loss curves of GLS and GLSO glass calculated with SRIM 2008. The energy loss of implanted ions in these two glasses is almost the same, except slight differences starting at $9.5 \mu\text{m}$. However, the Δn_i , Δn_d , and the barrier positions of these two waveguides are different, which may be due to the different compositions of two kinds of glasses. By comparing Fig. 5.1.2 and Fig. 5.1.4, it can be seen clearly that the enhanced refractive index wells are mainly located in the electronic damage regions, whilst the barriers are formed in the nuclear damage regions. The barrier formation has been widely accepted to be due to the collisions between the incident ions and target nuclei (nuclear damage) [16-18], which causes major structural damages. Though the fluence in this work is ultralow, the nuclear energy loss of each incident Ar ion is quite high due to its implantation energy and heavy mass. Thus, the total Ar ions can induce collision cascades and result in the barrier formation.

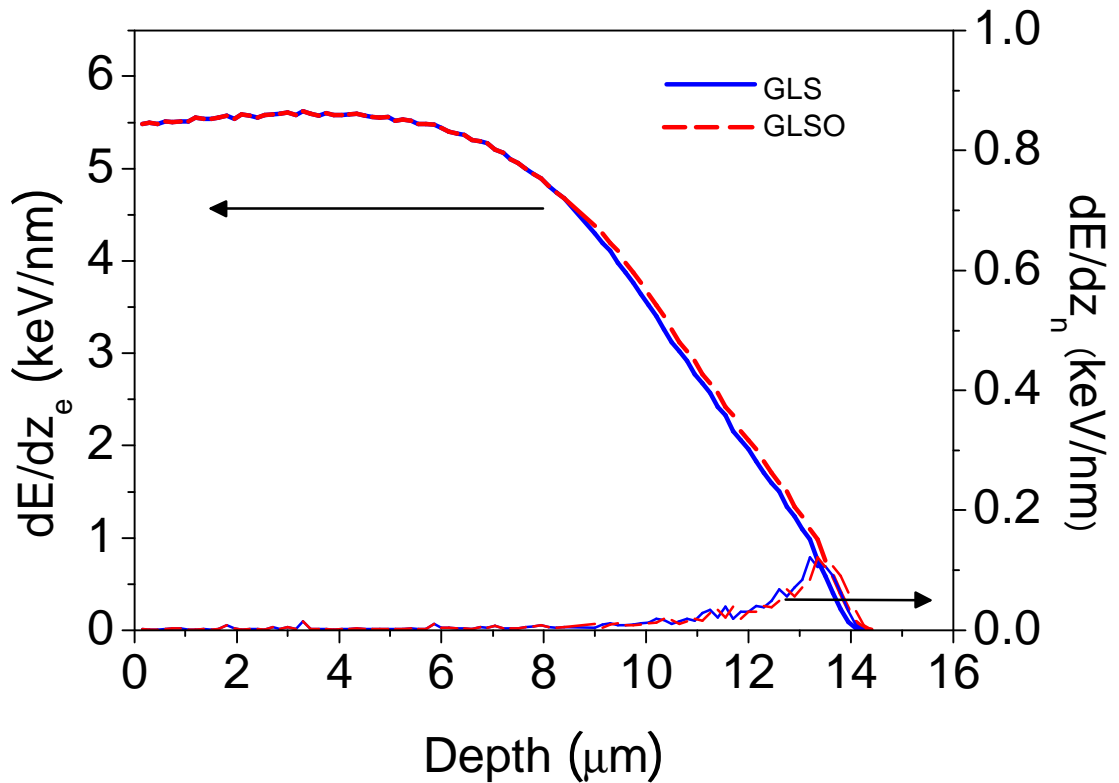


Fig. 5.1.4 Electronic energy loss (dE/dz_e) and nuclear energy loss (dE/dz_n)

As far as we know, there is no literature studying about the relationship between the electronic energy deposition and refractive index change in chalcogenide glasses. Some considerations can still be done, because amorphous chalcogenide thin films sometimes show photoinduced phenomena when irradiated with swift ions, such as photodarkening [19] and photobleaching [20]. Figure 5.1.5 shows the optical microscope photograph (measured by Keyence, VH-Z100R) of the cross section of the implanted GLSO sample. As is indicated, the implantation creates a surface layer of $11.50\mu\text{m}$ thick where the optical transmissivity is lower than the substrate. After annealing GLSO sample at $500\text{ }^\circ\text{C}$ (GLSO glass –transition temperature is $550\text{ }^\circ\text{C}$) for one hour, we found that the darker layer disappears. Moreover, the darkening layer is accompanied by refractive index enhancement. All results

above show that the “darkening” in our case is very similar to the reversible photodarkening which is an electronic effect described by means of configuration diagrams in literatures [21, 22]. The GLS sample exhibits the same “darkening” phenomenon as GLSO sample. Thus, according to the photodarkening mechanism [21, 22], the mechanism of enhanced index well formation in the GLSO and GLS samples is supposed as follows: the atoms in the substrate absorb energy from the implanted ions (electronic energy loss); the electrons are excited to higher energy levels and the atomic bonding is rearranged, thus the rearranged structure order causes the “darkening” and refractive index enhancement; the higher electronic energy levels are quasi-stable states which are stable at the room temperature but unstable near glass-transition temperatures. In Ref. 11, the authors suggest that the refractive index enhancement originates from the compaction change of silica, which is different from our case.

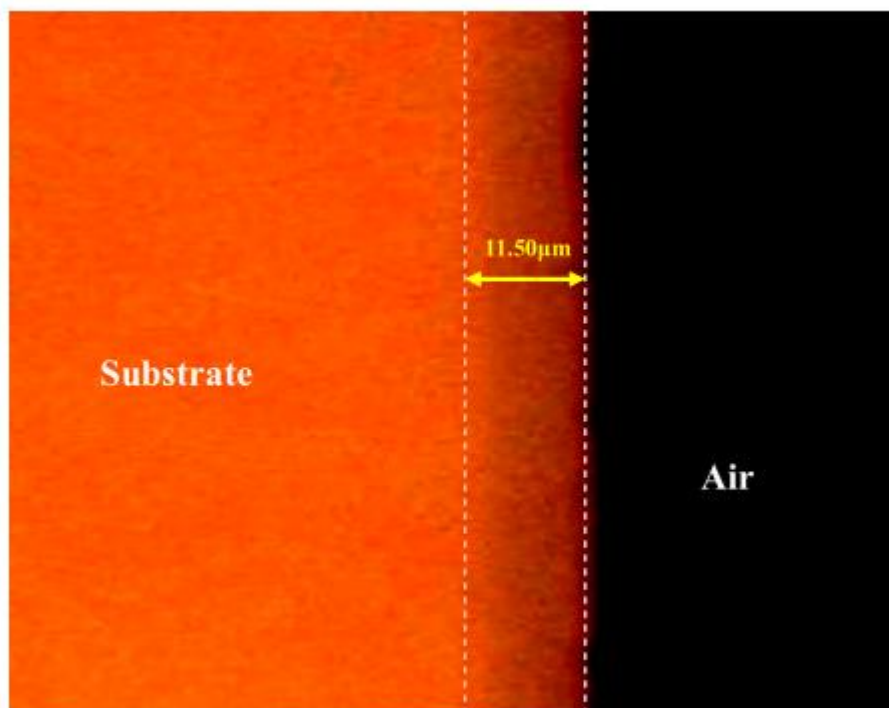


Fig. 5.1.5 Microscope photograph of the cross section of the Ar implanted GLSO waveguide

One of the most important features of a waveguide is its optical loss. The measurements in the present study result in the propagation loss of 2.0 dB/cm for GLS and 2.2 dB/cm for GLSO at the wavelength of 632.8nm.

5.1.4 Conclusions

The implantation with swift Ar ions of energy 60 MeV and fluence as low as 2×10^{12} ions/cm² is used to produce optical waveguides in GLS and GLSO glass. The waveguides have a “well+ barrier” type refractive index distribution and non-leaky mode formations. It is supposed that a “darkening” phenomenon accompanying the refractive index enhancement is caused by a subtle change in the structure order of the substrates. The waveguides present reasonably low propagation loss of 2.0 dB/cm for GLS waveguide and 2.2 dB/cm for GLSO waveguide. Compared with the previous results of conventional ion implantation, swift ion implanted waveguides in present work possess the advantages of more effective fabrication process, larger refractive index change, non-leaky modes and lower propagation loss. We believe that swift ion implantation method has a great potential in fabrication of amorphous material waveguides.

5.2 Refractive index change mechanisms in swift -heavy ion implanted Nd:YAG waveguide

5.2.1 Introduction

Nd:YAG is an extensively used laser crystal. Ion implantation has been applied to realize waveguide lasers in this material [23-25] effectively. So far, most of ion implanted Nd:YAG waveguides have been fabricated utilizing the energy from hundreds keV to several MeV and a dose of $10^{15} - 10^{17}$ ions/cm² [24-27]. In these normal implantation cases, the damage caused by nuclear

collisions usually induces amorphous layer in Nd:YAG crystals and reduces the refractive index, which results in an optical barrier. The region between this barrier and the surface can act as a core of the planar waveguide.

Recently, swift and heavy ion implantation (SHI) has emerged to be a more effective method in fabricating waveguides due to its ultra-low dose [28-30]. Among SHI works, most attention has been given to LiNbO₃. As a result, the optical properties (such as refractive index distribution, photorefractive), the mechanism of waveguide formation and theoretical models fitted the experimental results have been obtained for LiNbO₃ [28, 30-34]. For the purpose of laser light generation, 60MeV Ar and 20MeV N ion implantations have been applied to realize optical waveguides in Nd:YAG crystals [10, 35]. In those work, buried waveguides have been generated, which is quite different from the cases of normal ion implanted Nd:YAG waveguides and swift and heavy ion implanted LiNbO₃ waveguides. However, the mechanisms of the waveguide formation and the detailed information of the refractive index distribution have not been analyzed.

In this part, we choose 20MeV N ions to fabricate a planar waveguide in Nd:YAG crystal. The relationship between crystal damage and the refractive index change are characterized, and the experimental results are compared with the thermal spike model.

5.2.2 Experimental

The Nd:YAG crystal (doped by 1 at. % Nd³⁺, 10 × 5 × 2 mm³) was irradiated with 20MeV N³⁺ with the fluence of 1.5 × 10¹⁴ ions/cm² (on one 10mm × 5mm surface), using tandem accelerator at Tokai Research and Development Center, Japan Atomic Energy Agency. The beam current density was maintained at as small as 100nA/cm² to minimize charging and heating effects during irradiation.

After the implantation, the dark-mode spectrum (632.8nm) of the waveguide was measured by the prism coupling method. The near field pattern was measured by an end-fire coupling system at the wavelength of 632.8nm. A Renishaw Ramascope setup was used for Raman back-scattering measurements.

5.2.3 Optical and Raman characterization

From the prism coupling spectrum (not shown here), no modes were observed and the surface refractive index is unchanged compared with the bulk. The measured near-field pattern (Fig. 5.2.1 (a)) verifies that a buried waveguide is produced. From Fig.5.2.1 (a), it can also be determined that the waveguide is 10 μm thick and centred at a depth of around 6.9 μm , which is consistent with the electronic energy loss (S_e) of incident N ions (Fig. 5.2.1(d)) [10] calculated by SRIM 2010 [36].

Figure 5.2.2(a) shows the Raman spectra of the most damaged region (point h in Fig. 5.2.2 (b)) and the non-irradiated substrate. The observed Raman modes in Fig. 5.2.2 (a) are in agreement with the ones reported by Papagelis et al. [37]. Just as shown in Fig. 5.2.2(a), we find that the feature of all Raman modes in the irradiated region shows an overall intensity reduction compared with non-irradiated substrate. Fig. 2(b) exhibits the depth profile of the Raman intensity of A_{1g}^1 mode, and other modes also have the same trend of changing with depth. Indeed, the Raman reduction at the damaged area has already been reported in femtosecond laser written Nd:YAG waveguides [38]. In that work, the damage was attributed to some degree of amorphization which may induce a refractive index change. It is natural that crystals show similarities under femtosecond-laser pulse and SHI (in the electronic stopping regime), because the main physical process is the massive excitation of electrons in both cases [39]. Therefore, we can conclude that some degree of amorphization causes the

refractive index change in the electronic damaged region (from point a to i in Fig. 5.2.2(b)) in the N^{3+} ion implanted waveguide.

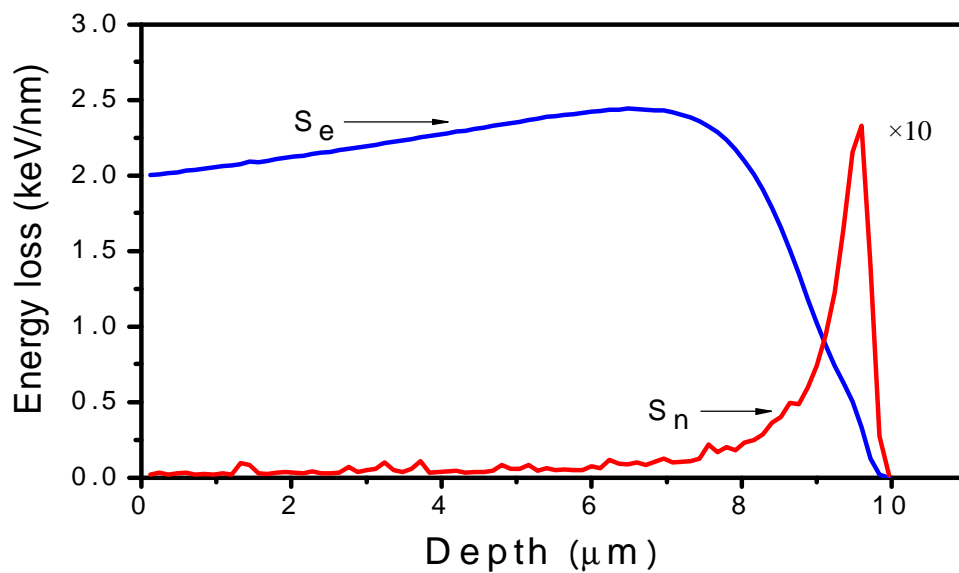
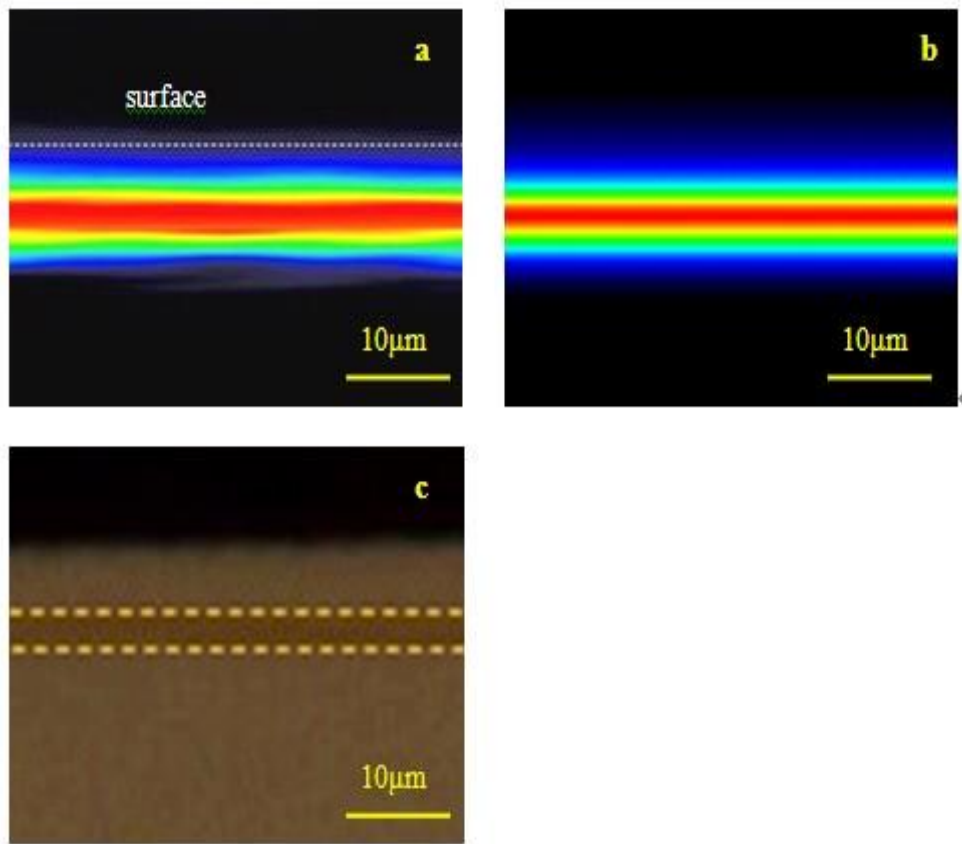


Fig. 5.2.1 Near-field patterns of the waveguide (fundamental mode) at the wavelength of 632.8nm (a) measured and (b) simulated. (c) Microscope photograph of the cross section of

the waveguide. (d) S_e and $S_n (\times 10)$ profile of incoming N ions.

The amorphization in crystals usually induces refractive index decrease, such as swift ion implanted LiNbO_3 [28] and KGW [40], and femtosecond laser written Nd:YAG [38]. However, the index of the waveguide in this work does not change at the surface and even increases below the surface, which is obviously different from the above cases. Here, it is suggested that an intrinsic threshold of damage exists in Nd:YAG crystal. The index will increase when the damage is below the threshold. In fact, the “threshold” conception is not surprising, as it can also be found in normal ion implanted Nd:YAG waveguides. Prior works by P. D. Townsend et al. have reported that 2MeV He ions can produce a refractive index enhancement in the nuclear damage region when the implanted dose was 1.5×10^{16} ions/cm², but reduction with dose larger than that [10, 26]. In addition, focused ion beam writing can also cause positive refractive index change in the nuclear damage region in Nd:YAG [41]. The refractive index enhancements in those works and present case can both be attributed to the damage caused by implanted ions lower than the threshold.

According to the near field pattern and the Raman intensity depth distribution, we choose the method in Ref. 10 to reconstruct the refractive index profile (Fig. 5.2.3(a)). The fundamental mode of the waveguide was simulated assuming various refractive index profiles by means of the beam propagation method using the software BeamPROP [42]. We can estimate the realistic index distribution when a good agreement is obtained between the simulated mode and experimental one. Fig. 5.2.1(b) shows the simulated fundamental mode when the index profile is assumed as in Fig. 5.2.3(a). As we can see in Fig 5.2.1(a) and (b), a good agreement has been obtained, indicating the assumed refractive index distribution agrees with the real one. From the refractive index profile and the Raman intensity depth distribution, it can be concluded: (1) the refractive index has a larger increase when the crystal damage is heavier. (2)

For the index change (crystal damage), S_e is dominant in the first several micrometers, while S_n also plays a key role near the end of ion range.

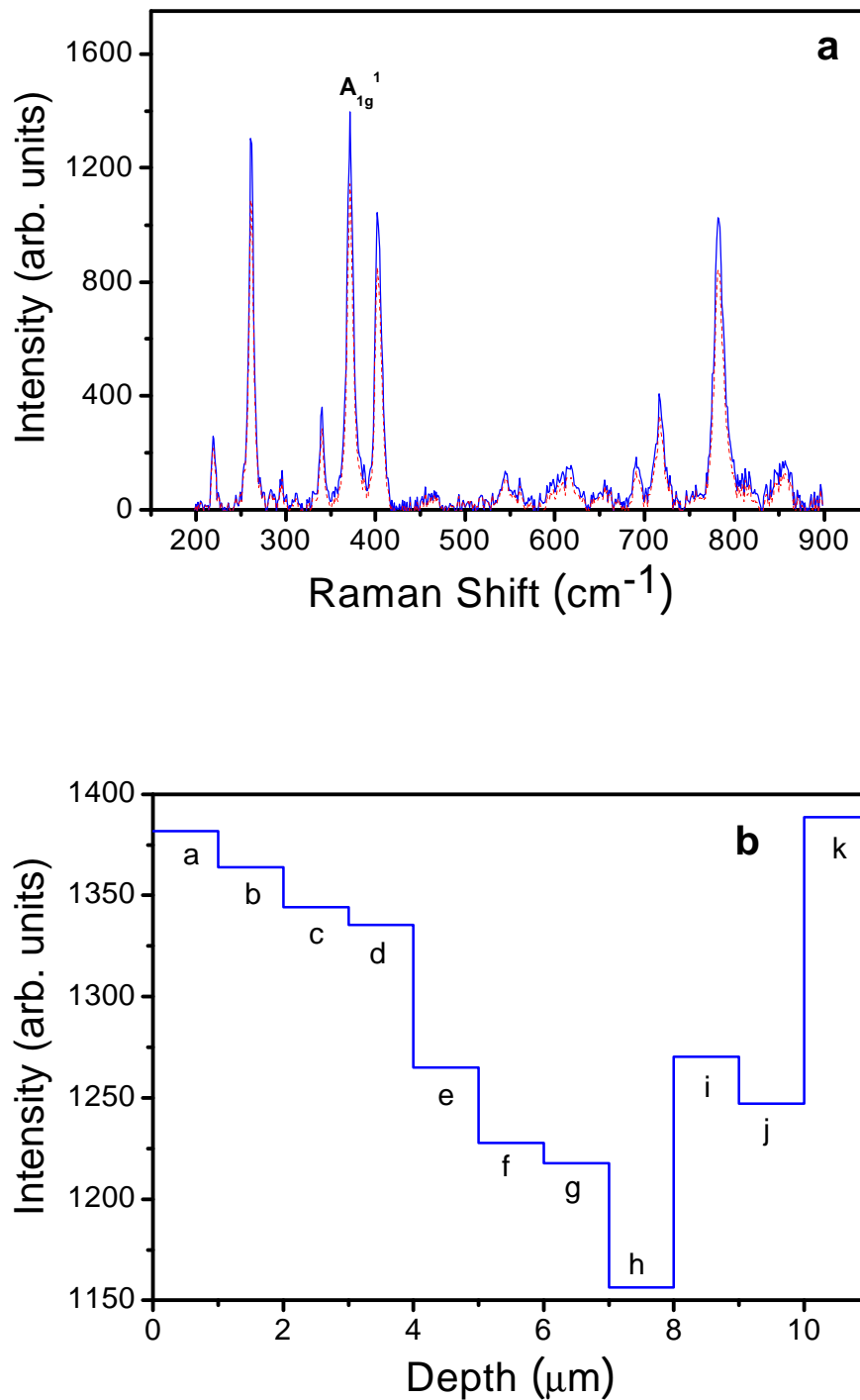


Fig. 5.2.2 (a) Raman spectra of the point 7~8μm (red dash line) and the non-irradiated substrate (blue line) (b) Depth profile of the Raman intensity of A_{1g}¹ mode (the point k corresponds to the substrate).

5.2.4 Theoretical damage comparison

In this part, we calculate the damage distribution approximately in the N^{3+} ion implanted waveguide by the thermal-spike model, and compare it with the result obtained from refractive index change and Raman spectra. As mentioned in section 2.3, basic equations in the thermal-spike model are

$$\Delta T_{\max}(r, S_e) = \frac{gS_e}{2pa_0^2 rC} e^{-r^2/2a_0^2}, \quad 0 < r < \sqrt{2} a_0 \quad (1)$$

$$\Delta T_{\max}(r, S_e) = \frac{gS_e}{perC} \frac{1}{r^2}, \quad r > \sqrt{2} a_0 \quad (2)$$

$$c(T) = Ae^{-e/KT} \quad (3)$$

$$\bar{c}(f, S_e) = 2pf \int_0^\infty rc[T_{\max}(r, S_e)]dr \quad (4)$$

where $\Delta T_{\max} = T - T_s$, T_s being the substrate temperature, g is efficiency of energy transfer from the electronic system to the lattice, a_0 the width of the initial Gaussian distribution, ρ the crystal density, C the specific heat, r the distance from the impact point (only in the input surface), $c(T)$ intrinsic defects generated by one implanted ion, f the irradiation dose, and $\bar{c}(f, S_e)$ is the average defect concentration after the fluence f . Here, we choose $a_0 = 4.5\text{nm}$, which is suitable for a variety of insulator crystals [32, 43]. Thus, the only relevant parameters are g and ε . Due to the close similarity of the YAG and YIG (yttrium iron garnet) crystal-chemical structure [44], the value of g is assumed as 0.35 following the ion irradiated YIG model and experiments [43]. The kinds of defects formed in irradiated crystals are very complicated. In the works of LiNbO_3 , the model fits the experiments well when ε is 0.34 – 0.63eV [33, 45]. This value is comparable with the calculated minimum formation energy of Frenkel defects (0.93eV) [46]. In fact, F. Agulló-López et al. have mentioned the atom displacement and Frenkel pair formation if the excited electron

overcomes the energy barrier ε [33]. According to the minimum formation energy of Frenkel defects in YAG crystal [43], ε is estimated as 4.88eV. As a result, the normalized damage (supposed the maximum $\bar{c}(f, S_e)$ as 1) can be easily determined through the equations above, and the result is shown in Fig. 5.2.3(b).

The crystal damage caused by SHI can also be associated with the refractive index change through effective medium method [30, 47]. In this method, the square of the refractive index (n^2) can be written,

$$n^2 = n_s^2 - \Delta n f_{dam}(d) \quad (5)$$

where n_s is the refractive index of the substrate, $f_{dam}(d)$ the normalized fraction of the damaged material at different depth and Δn is the refractive index decrease when $f_{dam}(d)$ is maximum. Therefore, $f_{dam}(d)$ can be determined through the refractive index change (Fig. 3(a)), and the calculated result is also shown in Fig. 5.2.3(b).

By comparing the two curves in Fig. 5.2.3(b), it can be seen clearly that the agreement is well up to 6.5um, which confirms the conclusion that S_e is dominant in the first several micrometers. The deviation from 6.5um to the end is caused by S_n . This is consistent with the calculated S_n which starts to increase obviously from around 7um (Fig.5.2.1 (d)). Moreover, it is worth noting the value of ε in the thermal-spike model. Though only one kind of defect is considered and the value of ε is at room temperature, the agreement of the two curves in the first 6.5um shows that this value is reasonable. This suggests that the effect of temperature change on ε is not very important and the main defects are Frenkel pairs. Nevertheless, further investigation is needed to understand the defect formation better.

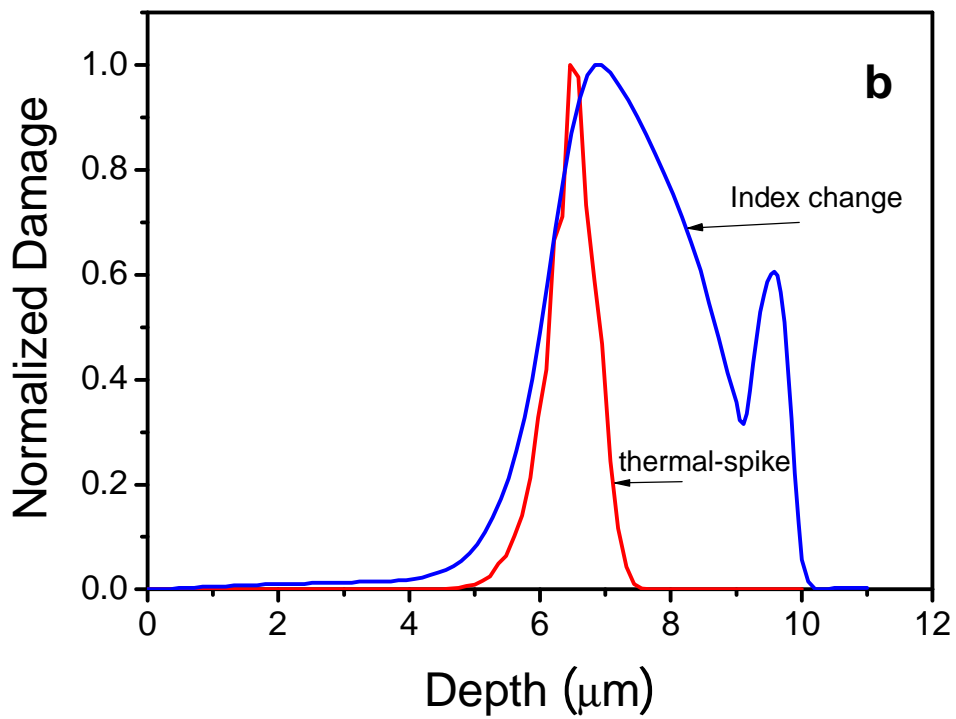
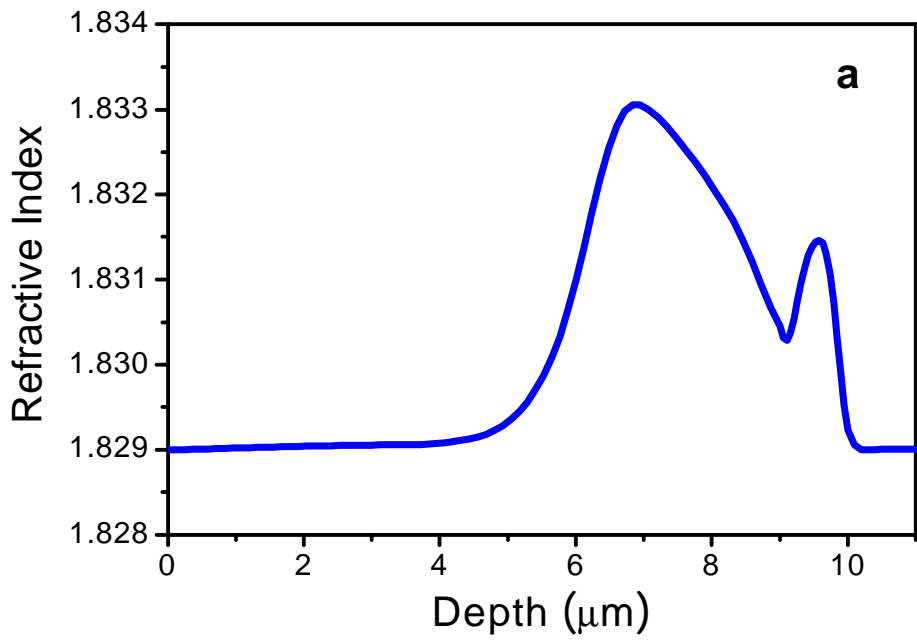


Fig. 5.2.3 (a) Refractive index profile of the N implanted Nd:YAG waveguide. (b) Damage distribution calculated by thermal-spike mode and refractive index change.

5.2.5 Conclusions

Nd:YAG buried planar waveguide has been fabricated by 20MeV ions with the dose of 1.5×10^{14} ions/cm². The refractive index profile has been reconstructed based on the results of Raman spectra and near-field pattern. The relationship between the refractive index change and crystal damage has been discussed. From thermal spike model, it has been found that S_e dominates from the surface to about 6.5 μm and S_n also acts on the refractive index increase near the end of ion range, which agrees with experimental results. This work is helpful to understand the mechanisms of swift-heavy ion implanted Nd:YAG waveguide formation.

5.3 Swift and Heavy Ion Implanted rare-earth doped GLS Laser Glass Waveguides and Their Different Refractive Index Distributions

5.3.1 Introduction

Waveguide lasers have received much attention because the waveguide structure can provide higher optical gain and lower threshold power than the bulk structure. At present, one of the research hotspots with respect to waveguide lasers is to explore novel hosts and transitions [48]. GLS glass reported by researchers at the University of Southampton [49, 50] is an ideal active host, due to its high glass transition temperature (580°C), high rare-earth dopant concentrations without clustering and greatly improved mechanical properties. Ho³⁺-doped GLS glass possesses the emission in near and mid- IR [51] and Nd³⁺-doped GLS glass has the laser output at 1.075 μm [52], which makes them attract considerable interest.

Crystal waveguides with good performance have been produced successfully

by swift-heavy ion implantation (SHI), and the application of SHI on glassy materials is also emerging. In Ref. 11, 5MeV F and 20MeV Cl ions have been used to fabricate waveguides in α -SiO₂. The waveguides show a step-like refractive index distribution (index enhancement). In section 5.1, 60MeV Ar have caused a “well + barrier” index distribution in GLS and GLSO glass waveguides, which is also convenient for waveguide structures but obviously different from the α -SiO₂ case.

The purpose of this work is to fabricate of planar waveguides in Ho or Nd doped GLS glasses by using either 60MeV Ar⁴⁺ ion implantation at an ultralow fluence or 20MeV N³⁺ ion irradiation at a moderate dose. The difference of refractive index distributions in the two cases is clarified to result from the different implanted dose.

5.3.2 Experimental

The molar compositions of the glasses (10mm × 10mm × 2mm) are 70Ga₂S₃:29.5La₂S₃:0.5Ho₂S₃ (Ho:GLS) and 5Ga₂S₃:31.4La₂S₃:3La₂O₃:0.6Nd₂S₃ (Nd:GLS). After cleaning, the glasses were implanted either with 60MeV Ar⁴⁺ with the fluence of 2×10^{12} ions/cm² or with 20MeV N³⁺ with the dose of 1.5×10^{14} ions/cm². After implantations, TE mode spectra of the waveguides were measured by the prism coupling method. The near field patterns were measured by an end-fire coupling system at the wavelength of 632.8nm. The back-reflection method was used to measure the propagation loss of the waveguides (632.8nm).

5.3.3 60MeV Ar implanted waveguides

The refractive indices of Ho:GLS glass and Nd:GLS glass are measured to be 2.4553 and 2.4830 at 632.8nm, and 2.3577 and 2.3811 at 1539nm, respectively (shown as n_{sub}). Figure 5.3.1 shows the dark-mode spectra of the Ar implanted

waveguides at 632.8nm. As one can see, for the Ho:GLS sample, only one sharp dip exists, which means that the waveguide can carry one mode (TE_0) whose effective refractive index (n_{eff}) is higher than n_{sub} . For the Nd:GLS sample, all dips are rather broad. Thus, it is necessary to examine the bright modes by end-fire coupling. Only two bright modes of the Nd:GLS waveguide were detected (Fig. 5.3.3 (d) and (e)), which indicates that the first two dips correspond to two modes and no other modes exist. Moreover, both waveguides can not support any mode at the wavelength of 1539nm.

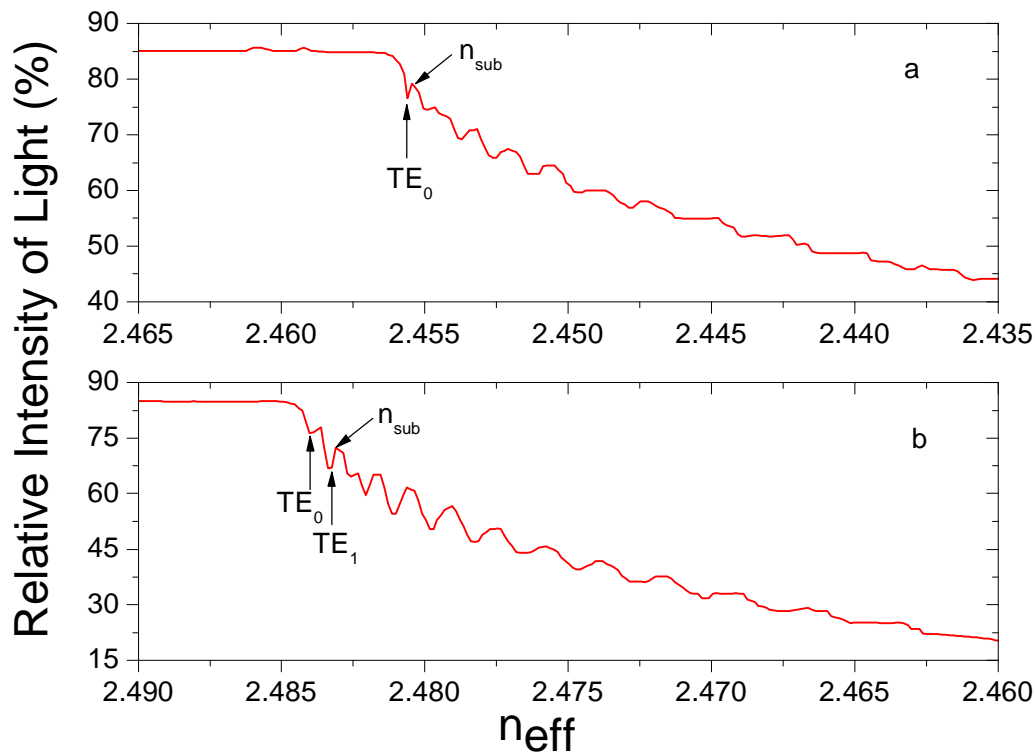


Fig. 5.3.1 TE mode spectra of Ar implanted (a) Ho and (b) Nd doped waveguides at 632.8nm

The refractive index profiles of the waveguides are reconstructed by RCM based on the data from the dark mode measurements. Figure 5.3.2 illustrates the refractive index profiles of Ho:GLS and Nd:GLS waveguides implanted with Ar ions. It is found that the measured n_{eff} s are in agreement with the calculated

values (based on Fig. 5.3.2) within 10^{-4} . For further confirmation of the refractive index distributions, we performed a modal simulation by using beam propagation method. Figure 5.3.3(a) – (d) depict the calculated and measured modal profiles of the TE₀ mode at 632.8nm. By comparing Fig. 3(a) and (b), and (c) and (d), we can conclude that the simulation agrees reasonably well with the experimental data.

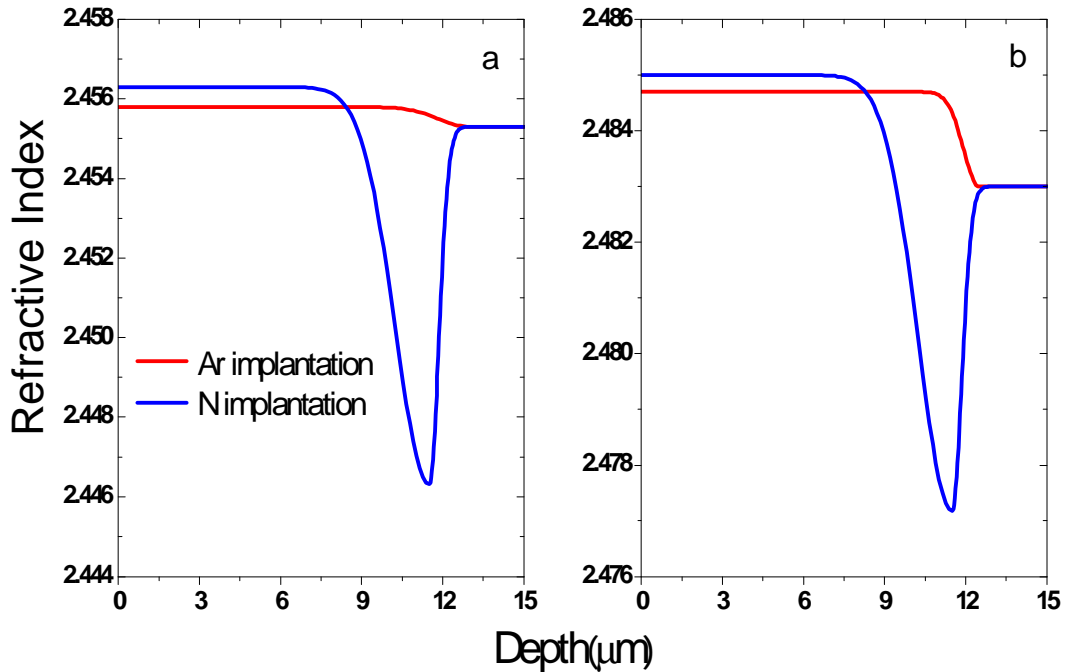


Fig. 5.3.2 The refractive index profiles of the Ar and N implanted waveguides at 632.8nm (a) Ho:GLS and (b) Nd:GLS

5.3.4 20MeV N implanted waveguides

Figure 5.3.4 and 5.3.5 show the dark-mode spectra of the N implanted Ho:GLS and Nd:GLS waveguides after annealing (see Discussion) at 632.8 and 1539nm. In Fig4 (a) and Fig. 5(a), the dip corresponding to the TE₀ mode is not very clear, which can be attributed to a very shallow low-index layer near the surface. This “missing” mode phenomenon has been observed for many other ion implanted waveguides, and it has been shown that this low-index layer can

be ignored. According to the number of sharp dips, we consider that there are six modes (TE_0 - TE_5) at 632.8nm, and two modes (TE_0 and TE_1) at 1539nm for both waveguides. The other dips are regarded as resonances.

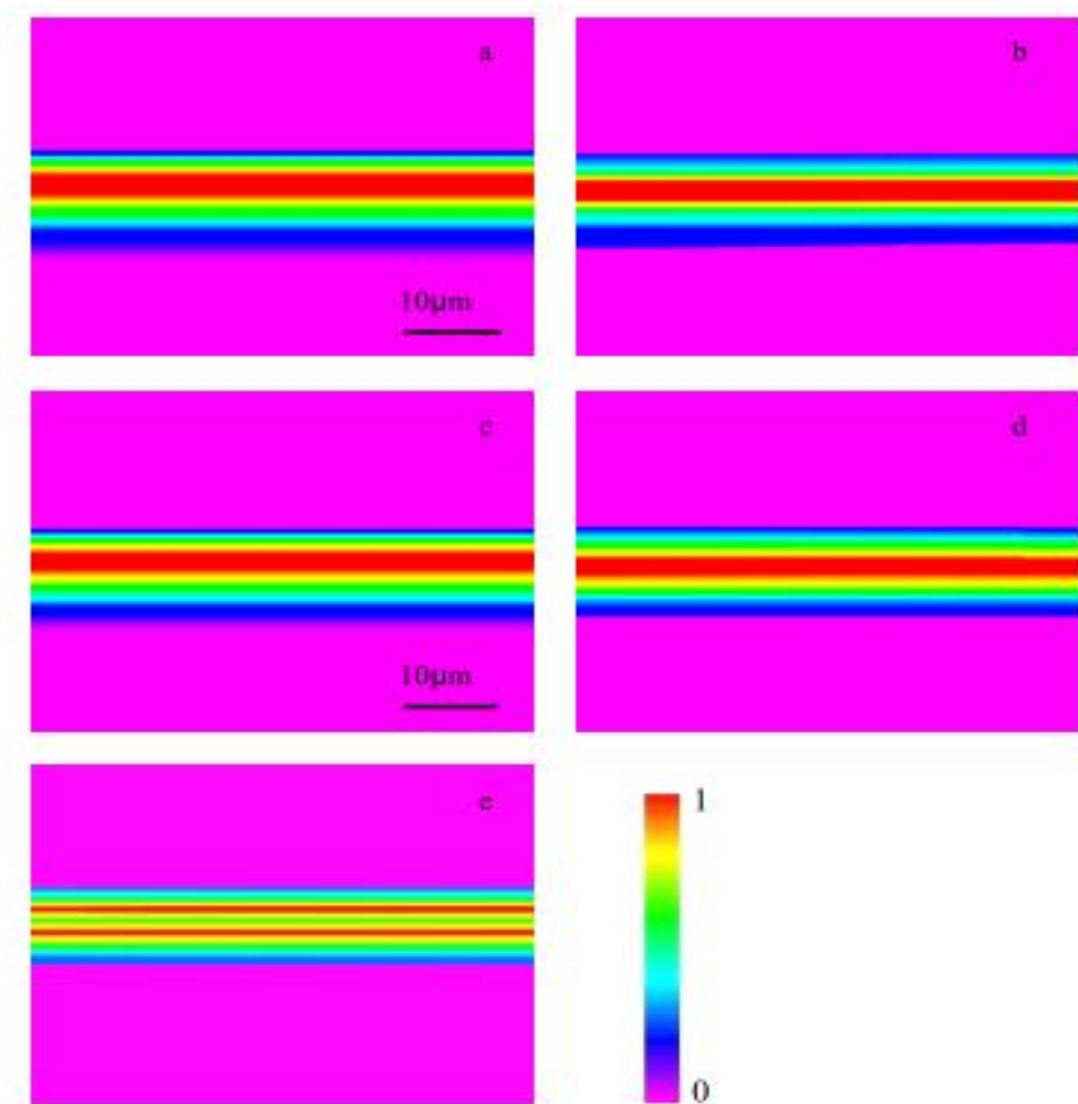


Fig. 5.3.3 Near-field patterns at the output plane of the Ho:GLS waveguide (a) simulated and (b) measured, and the Nd:GLS waveguide (c) simulated and (d) measured. The measured bright mode of TE_1 of the Ho:GLS waveguide is shown in (e).

The refractive index profiles are reconstructed at 632.8 and 1539nm by RCM as shown in Fig. 5.3.2 and 5.3.6. All profiles show a “well + barrier” shape: a well with positive index change is formed under the surface, and a barrier with negative index change is constructed between this well and the substrate. According to the index distributions at 632.8 and 1539nm, the refractive indices

of the samples at all other wavelengths can be calculated approximately by the Cauchy's equation $n=A+B/\lambda^2$.

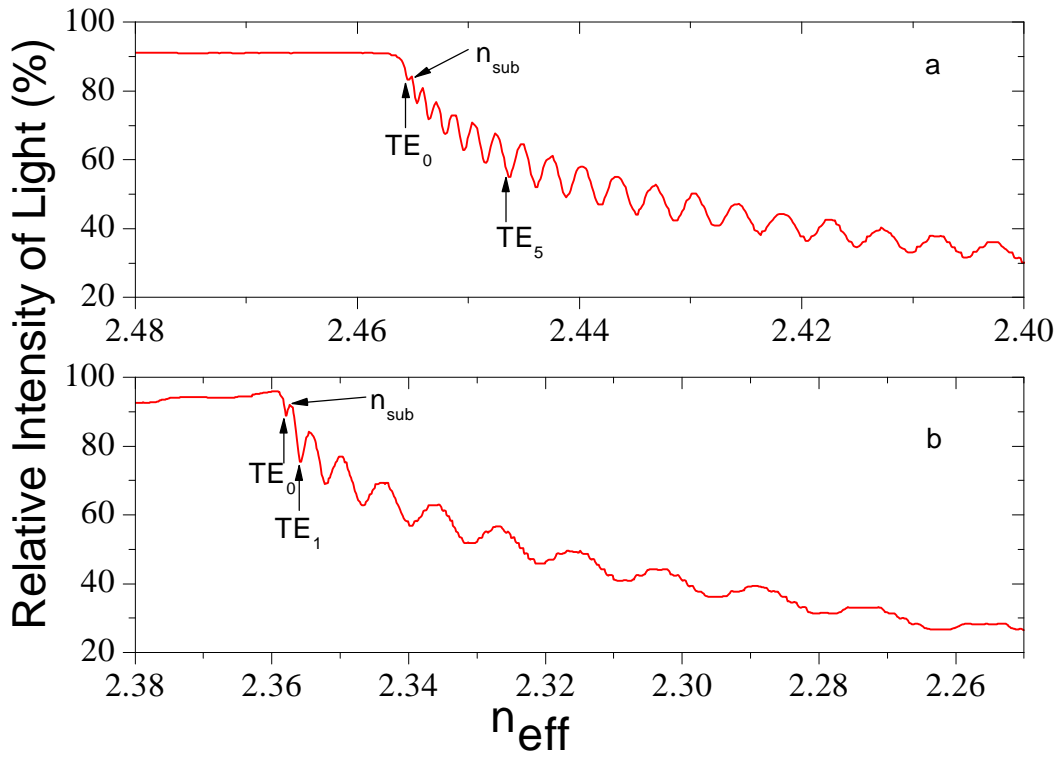


Fig. 5.3.4 TE mode spectra of the N implanted Ho doped waveguide at (a) 632.8nm and (b) 1539nm

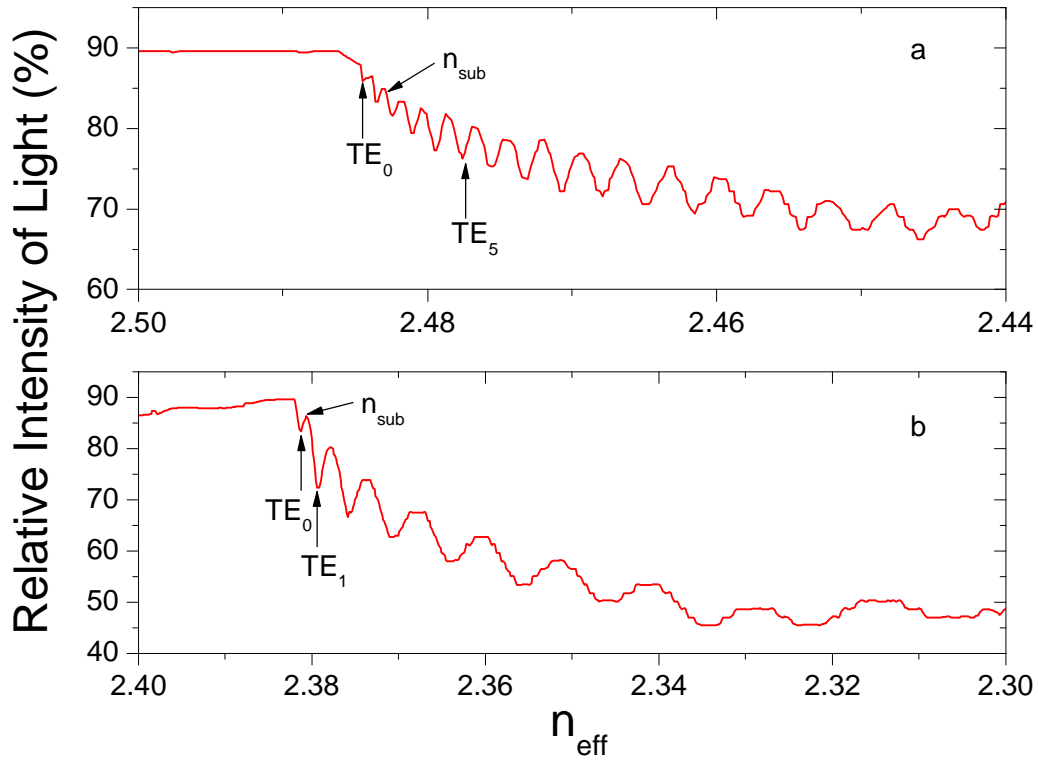


Fig. 5.3.5 TE mode spectra of the N implanted Nd doped waveguide at (a) 632.8nm and (b) 1539nm

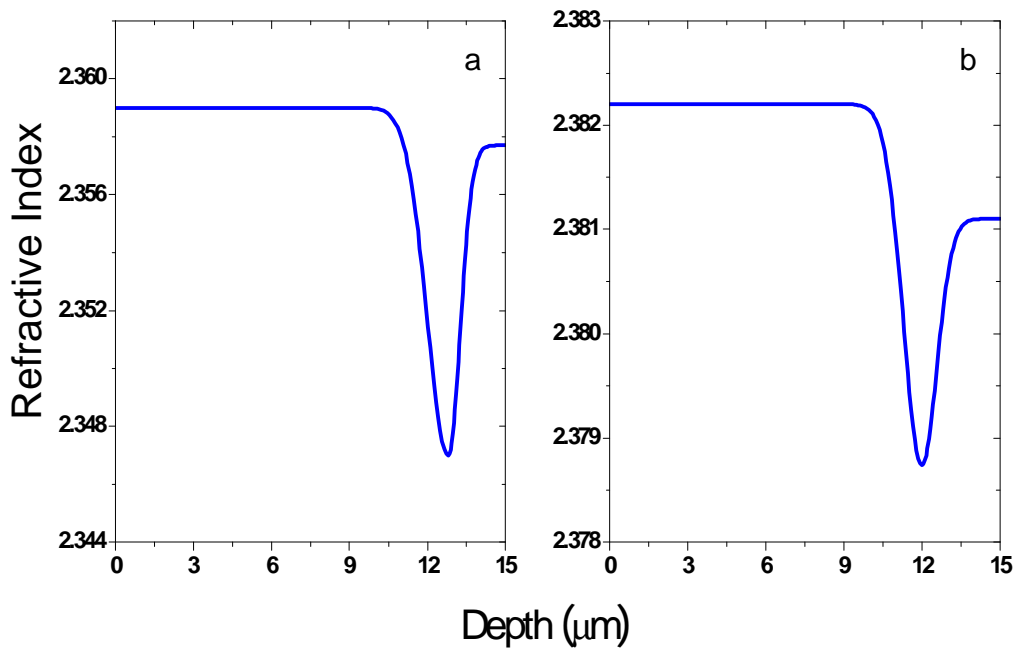


Fig. 5.3.6 The refractive index profiles of the N implanted waveguides at 1539nm (a) Ho:GLS and (b) Nd:GLS

5.3.5 Discussion of refractive index distributions

The mechanism of the waveguide formation in glass is usually complicated because of the complex composition and disordered structures of glass. Many studies about ion implanted glass waveguides imply that the nuclear energy loss (dE/dx_n) can induce refractive index decrease due to the collisions between implanted ions and atoms of the substrate [53, 54], although the detailed mechanism behind this is not clear yet. The electronic energy loss (dE/dx_e) can result in the darkening phenomenon in chalcogenide glasses, which is very similar to photodarkening. This phenomenon can lead to a refractive index change according to the Kramers-Kronig relations. The mechanism behind this darkening and index modifications may be the electronic structure change of the substrate [21].

Since the energy loss behaviour of implanted ions is similar in Ho:GLS and Nd:GLS glasses, calculated results are shown only for Ho doped glass in Fig. 5.3.7. For N implantation, by comparing Fig. 5.3.2 (or 5.3.6) with Fig. 5.3.7, it can be seen clearly that the enhanced refractive index areas are mainly located in the electronic damage regions, whilst the barriers are formed in the nuclear damage regions. As discussed above, the well and barrier formations is attributed to the dE/dx_e and dE/dx_n , respectively.

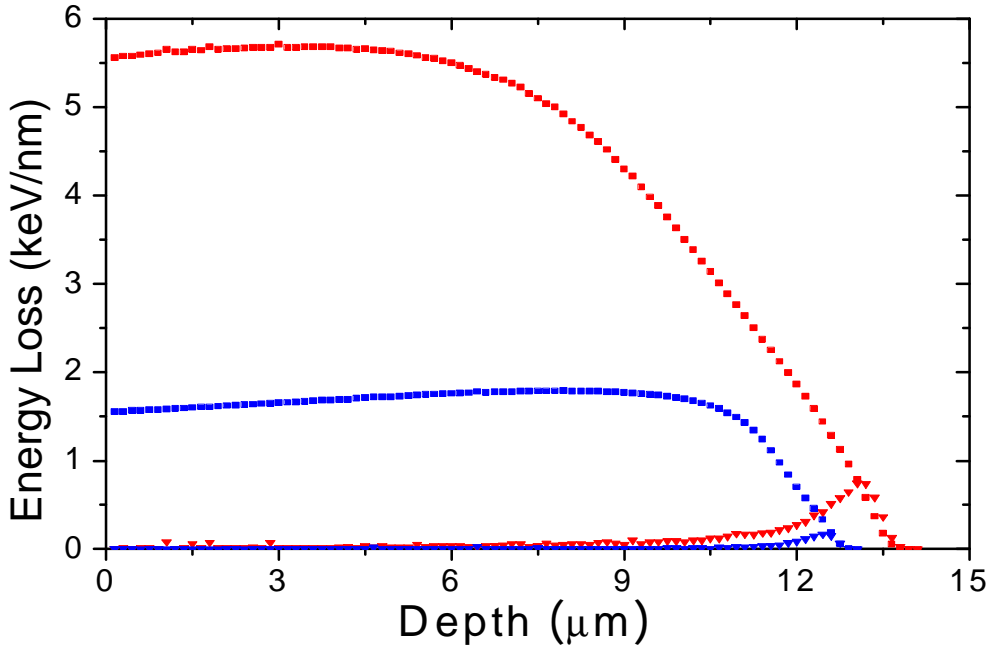


Fig.5.3.7 dE/dx_e (square) and dE/dx_n (triangle) of 60MeV Ar (red) and 20MeV N (blue) ions in Ho:GLS glass

For Ar implantation, the dE/dx_n of each ion is higher than that of N ion (Fig. 5.3.7). However, the dose of Ar ions is much lower, causing less collisions and thus very shallow barrier formation. Moreover, owing to this lower dose, the refractive index enhancement of every Ar implanted waveguide is smaller than that of corresponding N implanted waveguide. In order to apply these waveguides in IR range, higher energy or dose is needed for Ar implantation. In Ref. 11, the energy loss of F or Cl ions is comparable with our case and the dose is as high as 10^{14} ions/cm², nevertheless the waveguides show a step-like refractive index distribution. This is because both of two kinds of energy loss can bring about the compaction (index enhancement) of α -SiO₂ [18].

After the implantation, the propagation loss is larger than 10dB/cm at 632.8nm for the N implanted Ho:GLS and Nd:GLS waveguides, which may be due to the color centers induced by the incident N ions. After annealing at

100°C for 30min in air, the propagation loss is reduced to ~1.3dB/cm for the Ho:GLS waveguide and ~1.5dB/cm for the Nd:GLS waveguide.

The main factors that determine the total loss of a waveguide include: absorption, scattering, end-face polishing quality and tunneling. According to the measured transmission spectra of Ho or Nd doped GLS glass (not shown here for briefly), the 5F_5 band of Ho:GLS glass [51] and $^2H_{11/2}$ band of Nd:GLS glass [55] cause the loss coefficient of ~1.0dB/cm at 632.8nm, which means the material absorption should be responsible for the total loss of N implanted waveguides. Therefore, we believe that the N implanted waveguides could possess very low loss at the laser emission wavelengths.

5.3.6 Conclusions

The planar waveguides are fabricated in Nd or Ho doped GLS glass by SHI. The Ar and N ions implanted waveguides show different refractive index distributions of approximate step-like and “well + barrier” type, respectively. The factor induced this difference is the much lower dose of Ar implantation. The low propagation loss of N implanted waveguides indicates a possibility for producing waveguide lasers in these glasses by SHI.

References

1. F. Qiu and T. Narusawa, *Opt. Mater.* 33, 527 (2011).
2. F. Chen, *J. Appl. Phys.* 106(8), 081101 (2009)
3. J. Villarroel, M. Carrascosa, A. García-Cabañes, O. Caballero-Calero, M. Crespillo and J. Olivares, *Appl Phys B* 95, 429 (2009)
4. C. A. Merchant, P. Scrutton, S. García-Blanco, C. Hnatovsky, R. S. Taylor, A. García-Navarro, G. García, F. Agulló-López, J. Olivares, A. S. Helmy, and J. S. Aitchison, *IEEE J. Quantum Electron.* 45(4), 373 (2009)
5. A. García-Navarro, J. Olivares, G. García, F. Agulló-López, S. García-Blanco, C. Merchant, and J. S. Aitchison, *Nucl. Instrum. Methods Phys. Res. B* 249, 177 (2006)
6. J. Olivares, G. García, F. Agulló-López, F. Agulló-Rueda, A. Kling, and J. C. Soares, *Appl. Phys. A: Mater. Sci. Process.* 81, 1465 (2005)
7. J. Olivares, G. García, A. García-Navarro, F. Agulló-López, O. Caballero and A. García-Cabañes, *Appl. Phys. Lett.* 86, 183501 (2005)
8. J. Villarroel, M. Carrascosa, A. García-Cabañes, O. Caballero-Calero, M. Crespillo and J. Olivares, *Appl Phys B* 95, 429 (2009)
9. J. Olivares, A. García-Navarro, G. García, A. Méndez, F. Agulló-López, A. García-Cabañes, M. Carrascosa, and O. Caballero, *Opt. Lett.* 32, 2587 (2007)
10. Y. Y. Ren, N. N. Dong, F. Chen, A. Benayas, D. Jaque, F. Qiu, and T. Narusawa, *Opt. Lett.* 35, 3276 (2010)
11. J. Manzanoa, J. Olivares, F. Agulló-López, M.L. Crespillo, A. Moróño and E. Hodgson, *Nucl. Instrum. Methods Phys. Res. B* 268, 3147, (2010)
12. A. Zakery, S.R. Elliott: *J. Non-Crystal. Solids* 330, 1(2003).

- 13.F. Qiu, T. Narusawa, *Jpn. J. Appl. Phys.* 49, 092503 (2010).
- 14.R. Ramponi, R. Osellame and M. Marangoni: *Rev. Sci. Instrum.* 73, 1117 (2002).
- 15.P. J. Chandler and F. L. Lama: *Opt. Acta* 33, 127(1986).
- 16.F. Chen, X. L. Wang, X. S. Li, L. L. Hu, Q. M. Lu, K. M. Wang, B. R. Shi, and D. Y. Shen, *Appl. Surf. Sci.* 193, 92 (2002).
- 17.F. Chen, X. L. Wang and K. M. Wang, *Opt. Mater.* 29, 1523 (2007).
- 18.P. D. Townsend, P. J. Chandler, and L. Zhang, *Optical Effects of Ion Implantation* (Cambridge University Press, Cambridge, 1994).
- 19.M. S. Kamboj, G. Kaur, R. Thangaraj, and D. K. Avasthi, *J. Phys. D* 35, 477 (2002).
- 20.M. S. Kamboj, R. Thangaraj, D. K. Avasthi, and D. Kabiraj, *Nucl. Instrum. Methods Phys. Res. B* 211, 369 (2003).
- 21.S. Ducharme, J. Hautala, and P. C. Taylor, *Phys. Rev. B* 41, 12250 (1990).
- 22.K. Tanaka, *Jpn. J. Appl. Phys., Part 1* 25, 779 (1986).
- 23.F. Qiu and T.Narusawa, *Appl. Phys. B*, DOI 10. 1007
- 24.M. Domenech, G. V. Vazquez, E. Flores-Romero, E. Cantelar, and G. Lifante, *Appl. Phys. Lett.* 86, 151108 (2005).
- 25.E. F. Romero, G. V. Vázquez, H. Márquez, R. R. Rojo, J. Rickards, and R. T. Luna, *Opt. Express* 15, 8513 (2007).
26. L. Zhang, P. J. Chandler, P. D. Townsend, S. J. Field, D. C. Hanna, D. P. Shepherd, and A. C. Tropper, *J. Appl. Phys.* 69, 3440 (1991).
- 27.G. V. Vázquez, J. Rickards, G. Lifante, M. Domenech, and E. Cantelar, *Opt. Express* 11, 1291 (2003).
- 28.J. Olivares, G. García, A. García-Navarro, F. Agulló-López, O. Caballero, and A. García-Cabañes, *Appl. Phys. Lett.* 86, 183501 (2005).
- 29.J. Olivares, M. L. Crespillo, O. Caballero, M. D. Ynsa, A.

- García-Cabañes, M. Toulemonde, C. Trautmann and F. Agulló-López, *Opt. Express* 17, 24175 (2009).
30. T. Ruiz, A. Mendez, M. Carrascosa, J. Carnicero, A. Garcia-Cabañes, J. Olivares, F. Agullo Lopez, A. Garcia Navarro, and G. Garcia, *J. Phys. D: Appl. Phys.* 40, 4454 (2007).
31. J. Villarroel, M. Carrascosa, A. García-Cabañes, O. Caballero-Calero, M. Crespillo, and J. Olivares, *Appl. Phys. B: Lasers Opt.* 95, 429 (2009).
32. F. Agulló-López, G. García, and J. Olivares, *J. Appl. Phys.* 97, 093514 (2005).
33. F. Agulló-López, A. Méndez, G. García, J. Olivares, and J. M. Cabrera, *Phys. Rev. B* 74, 174109 (2006).
34. P. Kumar, S. M. Babu, S. Ganesamoorthy, A. K. Karnal and D. Kanijial, *J. Appl. Phys.* 102, 084905 (2007).
35. Y. Y. Ren, N. N. Dong, F. Chen, and D. Jaque, *Opt. Express.* 19, 5522 (2011).
36. J. F. Ziegler, computer code, SRIM <http://www.srim.org>.
37. K. Papagelis, G. Kanellis, S. Ves, and G.A. Kourouklis, *Phys. Status. Solidi (b)* 233, 134 (2002).
38. A. Ródenas, J. A. Sanz García, D. Jaque, G. A. Torchia, C. Méndez, I. Arias, L. Roso, and F. Agulló-Rueda, *J. Appl. Phys.* 100, 033521 (2006).
39. A. García-Navarro, F. Agulló-López, J. Olivares, J. Lamela, and F. Jaque, *J. Appl. Phys.* 103, 093540 (2008).
40. C. A. Merchant, P. Scrutton, S. García-Blanco, C. Hnatovsky, R. S. Taylor, A. García-Navarro, G. García, F. Agulló-López, J. Olivares, A. S. Helmy, and J. S. Aitchison, *IEEE J. Quantum Electron.* 45(4), 373(2009).
41. A. Benayas, D. Jaque, Y. Yao, F. Chen, A. A. Bettiol, A. Rodenas, and

- A. K. Kar, *Opt. Lett.* 35 (23), 3898 (2010).
42. Rsoft Design Group, Computer software BeamPROP version 8.0.
43. G. Szenes, *Phys. Rev. B* 52, 6154 (1995).
44. M. M. Kuklja, *J. Phys.: Condens. Matter* 12, 2953 (2000).
45. A. Rivera, J. Olivares, G. García, J. M. Cabrera, F. Agulló-Rueda, and F. Agulló-López, *Phys. Stat. Solidi A* 206(6), 1109 (2009).
46. H. Doonerberg, S. M. Tomlinson, C. R. A. Catlow, and O. F. Schirmer, *Phys. Rev. B* 40, 11909 (1989).
47. J. Olivares, A. García-Navarro, G. García, A. Méndez, and F. Agulló-López, *Appl. Phys. Lett.* 89, 071923 (2006).
48. J. I. Mackenzie, *IEEE J. Sel. Top. Quantum Electron.* 13, 626 (2007).
49. M. Hughes, W. Yang, and D. Hewak, *Appl. Phys. Lett.* 90, 131113 (2007).
50. J. A. Frantz, L. B. Shaw, J. S. Sanghera, and I. D. Aggarwal, *Opt. Exp.* 14, 1797 (2006).
51. T. Schweizer, B. N. Samsom, J. R. Hector, W. S. Brocklesby, D. W. Hewak, and D. N. Payne, *Infrared Phys. Technol.* 40, 329 (1999).
52. A. K. Mairaj, C. Riziotis, A. M. Chardon, P. G. R. Smith, D. P. Shepherd, and D. W. Hewak, *Appl. Phys. Lett.* 81, 3708 (2002).
53. S. L. Li, K. M. Wang, F. Chen, X. L. Wang, G. Fu, Q. M. Lu, L. L. Hu, D. Y. Shen, and H. J. Ma, *J. Phys. D* 38, 2899 (2005).
54. L. Wang, F. Chen, X. L. Wang, K. M. Wang, Y. Jiao, L. L. Wang, X. S. Li, Q. M. Lu, H. J. Ma, and R. Nie, *J. Appl. Phys.* 101, 053112 (2007).
55. A. K. Mairaj, A. M. Chardon, D. P. Shepherd, and D. W. Hewak, *IEEE J. Sel. Top. Quantum Electron.* 8, 1381 (2002).

Chapter 6 Conclusions

In this thesis, we have presented the fabrication and characterization of ion implanted waveguides in GLS glasses and Nd:YAG crystals. Especially, ion implantation is applied on GLS glass waveguides for the first time. Several different measurement techniques have been used to analyze the resulting waveguides. The main results are summarized as follows:

1. Planar waveguide in GLS glass is fabricated by 350keV proton implantation. Two TE modes exist in the waveguide at 632.8nm. The surface refractive index of the implanted sample is only slightly larger than the substrate, and refractive index decreases by about 0.5% at the barrier which is located about 2.9 μm beneath the surface. The implanted sample shows good transmission at the wavelength range of 1.28-10 μm . The optical loss of the present waveguide is estimated to be about 3.2 dB/cm, which is a reasonable value and can be improved by annealing.
2. Based on proton implanted GLSO glass waveguides, we design and fabricate a Ti:GLSO glass waveguide by double proton implantation. The sample is implanted by 470keV proton with the dose of 1×10^{16} ions/cm² and then 500keV proton with the dose of 2×10^{16} ions/cm². The refractive index increases slightly in the guiding region and the barrier with negative index change is about 3 μm thick. All the light is confined in the guiding region due to the barrier thick enough, which is consistent with our prediction. According to micro-Raman spectra, the volume expansion mainly results in the barrier formation in the proton implanted Ti:GLSO waveguide. Moreover, the Raman intensity between the guiding region and

substrate is only slightly different and the propagation loss is about 0.5dB/cm, which are necessary conditions for future realization of waveguide lasers in Ti::GLSO glass.

3. We demonstrate the application of swift and heavy ion implantation to generate optical waveguides in chalcogenide glasses. GLS and GLSO glasses were irradiated with Ar⁴⁺ at 60 MeV and 2×10^{12} ions/cm². One and three non-leaky modes exist for GLS and GLSO glass waveguides respectively. Both waveguides exhibit the “well + barrier” refractive index distributions. The well confined light propagation shown by near-field patterns strongly suggests a possibility of channel waveguide fabrication by simply applying standard photolithographic procedures. By comparing the relevant electronic and nuclear energy loss curves and refractive index distributions, we conclude that the enhanced refractive index wells are mainly located in the electronic damage regions, whilst the barriers are formed in the nuclear damage regions. It is also supposed that a “darkening” phenomenon accompanying the refractive index enhancement is caused by a subtle change in the structure order of the substrates.
4. A buried planar Nd:YAG waveguide has been fabricated by 20MeV N ion implantation. We find that the feature of all Raman modes in the irradiated region shows an overall intensity reduction compared with non-irradiated substrate. This intensity reduction is attributed to some degree of amorphization in the implanted crystal. According to micro-Raman spectra, it is exhibited that electronic (S_e) and nuclear (S_n) damages both cause positive index change in the waveguide. From thermal spike model, it has been found that S_e dominates from the surface to about 6.5um and S_n also acts on the refractive index increase near the end of ion range, which agrees with experimental results.

5. The planar waveguides have been fabricated in Ho or Nd doped GLS laser glasses by 60MeV Ar or 20MeV N ion implantation. For 60MeV Ar implanted waveguides, one and two modes exist in Ho and Nd doped GLS glass waveguides respectively. Both waveguides can not support any mode at the wavelength of 1539nm. The refractive index profiles of both waveguides reconstructed by RCM show a step-like distribution. For 20MeV N implanted waveguides, there are six modes (TE_0 - TE_5) at 632.8nm, and two modes (TE_0 and TE_1) at 1539nm for both waveguides. All profiles show a “well + barrier” shape: a well with positive index change is formed under the surface, and a barrier with negative index change is constructed between this well and the substrate. The factor induced this difference between Ar and N implanted waveguides is the much lower dose of Ar implantation. Moreover, the low propagation loss of N implanted waveguides indicates a possibility for producing waveguide lasers in these glasses by swift heavy ion implantation.

Publications

1. **F. Qiu** and T. Narusawa, “Application of swift and heavy ion implantation to the formation of chalcogenide glass optical waveguides,” *Opt. Mater.* 33, 527 (2011)
2. **F. Qiu**, T. Narusawa and J. Zheng, “Swift and heavy ion implanted chalcogenide laser glass waveguides and their different refractive index distributions”, *Appl. Opt.* 50 (5), 733 (2011)
3. **F. Qiu** and T. Narusawa, “Refractive index change mechanisms in swift -heavy ion implanted Nd:YAG waveguide”, *Appl. Phys. B*, DOI: 10.1007/s00340-011-4606-0
4. **F. Qiu** and T. Narusawa, “Ion implanted Ti doped chalcogenide glass waveguide as a candidate of tunable lasers”, *J. Opt. Soc. Am. B* 28 (6), 1490 (2011)
5. **F. Qiu** and T. Narusawa, “Proton-implanted planar waveguide in gallium lanthanum sulphide glass,” *Jpn. J. Appl. Phys.* 49, 092503 (2010)
6. **F. Qiu** and T. Narusawa, “Swift ions implanted optical waveguides in chalcogenide glass”, *Proc. CAARI 2010*

Acknowledgements

I would like to thank everyone who helped me with this project. In particular, I would like to thank my supervisor Prof. Tadashi NARUSAWA for his giving me such a chance to study here, his attention and care all the time and his technical support and guidance. I would also like to thank Prof. A. Hatta and Prof. K. Nonaka for their assistance with optical measurement instruments. Thanks to all IRC member for their help in my ordinary life. At last, I would like to thank my beautiful wife.